

## ABSTRACT

Title of Thesis:     RECTIFICATION PERFORMANCE OF  
                          ANTENNA COUPLED MIM TUNNEL DIODES

Nicholas Kratzmeier, Master of Science, 2013

Thesis directed by:  Professor Martin Peckerar  
                          Department of Electrical  
                          and Computer Engineering

This thesis studies the use of antenna coupled metal-insulator-metal (ACMIM) tunneling diodes for long wave infrared (LWIR) energy harvesting applications. Bow tie shaped ACMIM structures provide good polarization and bandwidth response, coupling the incident radiation to the demodulating MIM tunneling diode for power rectification. The use of geometric asymmetry at the junction (one tip flat, the other pointed) and the resulting electric field enhancement provides the necessary current-voltage (IV) relationship asymmetry. This geometric technique allows a simultaneous reduction in resistance and capacitance, improving frequency response. These results were confirmed by finite-element analysis of fabricated structures, and optimized for  $10\mu m$  LWIR radiation. During testing, the device IV plots became linear (yet responded better), due to the electric field formation of a shunt resistance across the junction. Equivalent circuit models of the ACMIM structure were developed to study the effects of this shunt and understand the increased performance through impedance matching.

RECTIFICATION PERFORMANCE OF ANTENNA COUPLED  
MIM TUNNEL DIODES

by

Nicholas Matthew Kratzmeier

Thesis submitted to the Faculty of the Graduate School of the  
University of Maryland, College Park in partial fulfillment  
of the requirements for the degree of  
Master of Science  
2013

Advisory Committee:  
Professor Martin Peckerar/Advisor  
Professor Mario Dagenais  
Professor Christopher Davis

© Copyright by  
Nicholas Kratzmeier  
2013

## Acknowledgements

I would like to first off thank my advisor, Professor Martin Peckerar for his direction and support throughout this project. It has been a great experience learning from such a knowledgeable mentor who has helped me grow as a researcher.

I would also like to thank the other committee members, Professors Chris Davis and Mario Dagenais for their time in critiquing this thesis and its defense.

I thank my lab mates, Gavin Liu, Chao Wang, Wei Zhao, Jing Xia, Scott Bauman, and especially Dr. Filiz Yesilkoy. She has guided me throughout this project in the simulations, and I appreciate her patience in me producing useable results for her dissertation. I would also like to thank her for many of the pictures used in this work.

Next, I would like to thank the employees of CoolCAD Electronics for their insightful discussions concerning this project over the past year.

I have had a great time as both a graduate and undergraduate here at the University of Maryland, College Park. I would like to thank all the professors whose classes I have taken and inspired me to do my best. I have learned a lot, and am looking forward to moving on into a career in industry.

Finally, I would like to thanks all my friends and family for their continued support over the years, especially my parents, Hans and Michele, my siblings, Andrew and Christina, and girlfriend Sabina.

# Table of Contents

1	Introduction	1
1.1	Motivation . . . . .	2
1.2	Infrared Energy Harvesting from Terrestrial Radiation . . . . .	3
1.3	ACMIM Tunnel Diode Design Specifications . . . . .	6
1.4	Thesis Contribution . . . . .	9
1.5	Thesis Organization . . . . .	10
2	Background	11
2.1	Tunneling Methods . . . . .	11
2.2	Geometric Field Enhancement . . . . .	14
2.3	Antenna Design . . . . .	17
2.4	Previous Fabrication and Experimental Results . . . . .	21
2.5	Summary . . . . .	22
3	Finite Element Simulation Results	24
3.1	Electrostatic Simulation Results . . . . .	24
3.1.1	Mesh Density Analysis . . . . .	25
3.1.2	Tip Radius Analysis . . . . .	27
3.1.3	Gap Width Analysis . . . . .	31
3.1.4	Flare Angle Analysis . . . . .	33
3.1.5	Capacitance Analysis . . . . .	37
3.1.6	Imperfection Effects . . . . .	40
3.2	Electromagnetic Simulation Results . . . . .	42
3.2.1	Antenna Length Optimization . . . . .	46
3.2.2	Polarization Effects . . . . .	49
3.2.3	Substrate and Air Coupling Comparison . . . . .	51
3.3	Summary . . . . .	53
4	Equivalent Circuit Model Simulation Results	55
4.1	Equivalent Circuit Models . . . . .	55
4.1.1	Antenna . . . . .	55
4.1.2	Diode . . . . .	56
4.1.3	ACMIM with Measurement . . . . .	57
4.2	Shunt Resistance . . . . .	58
4.3	Impedance Matching . . . . .	59
4.4	Frequency Response . . . . .	65
4.5	Summary . . . . .	69
5	Conclusions and Suggestions for Further Work	71
	Bibliography	74

## Chapter 1

### Introduction

Energy harvesting has undergone extensive research in recent years as society pushes for products designed with sustainability in mind. One such source of energy comes from the earth emitting radiation in the infrared (IR) spectrum. To harness this energy, an antenna coupled diode (often referred to as a rectenna) is often used in conjunction with DC filters and power distribution networks, shown in Figure 1.1.

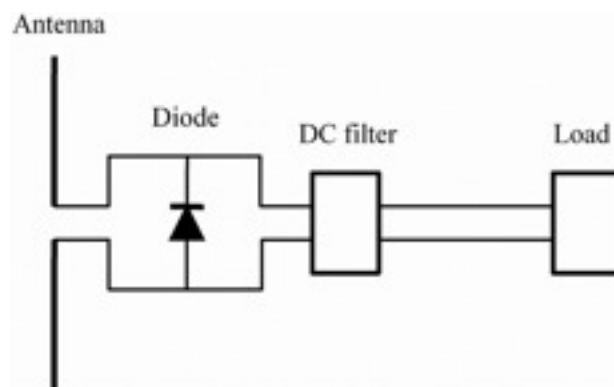


Figure 1.1: Rectenna energy harvesting system [7]

Rectennas integrate the demodulating diode within the physical antenna. The antenna couples AC power from the ambient environment and loads the diode which in turn rectifies the signal, giving a DC output. By integrating both the demodulator and antenna, we can achieve extremely small devices with minimal parasitic capacitive and resistive elements. The signal pathway is also physically shortened,

giving an improved signal-to-noise ratio (SNR). For the IR spectrum, an attractive demodulator is the Metal-Insulator-Metal (MIM) tunneling diode due to the extremely fast rectification through tunneling mechanisms that allow it to operate at the desired terahertz frequencies. A complete Antenna Coupled MIM (ACMIM) structure (using a bow tie antenna) can be seen in Figure 1.2.

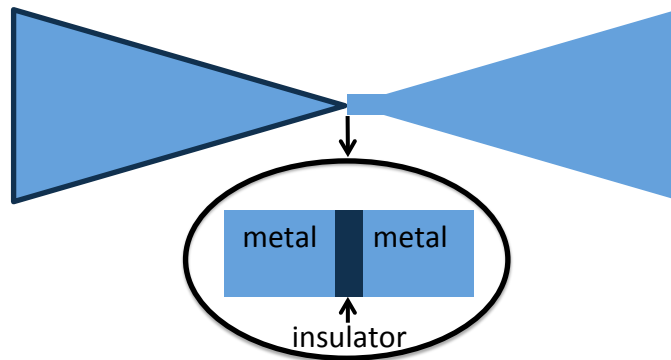


Figure 1.2: ACMIM tunnel diode

## 1.1 Motivation

In addition to IR energy harvesting applications, ACMIM diodes can also be used for simple IR detection. In these two scenarios, the difference in operation lies mainly with the diode DC bias. In order to not expend energy while trying to harvest energy, the ACMIM device must be operated at zero bias. However, for an IR detection application, the bias point can be tuned for operation at the device's highest point of responsivity (the "diode knee") leading to greater detection efficiency. Due to this operational difference, using the ACMIM diode as an energy harvester leads to greater challenges. The rectification behavior is determined by

the asymmetric current-voltage relation at zero-bias, which will be sub-optimal in comparison to that at the highest point of responsivity. Despite the limitations, the devices analyzed in this thesis can be used for both applications.

There exists a large demand for cheap and efficient IR detectors that operate at room temperature [19]. The IR detector market caters to a wide range of industries, from military (surveillance and target detection) to civilian, and research applications, such as space observatories. In terms of energy harvesting, capturing Earth's reradiating energy concentrated around a wavelength of  $10\mu m$  has been discussed since Bailey proposed harnessing the solar energy using RF rectification techniques in 1972 [11] and has continued to thrive. The first recorded use of fast MIM tunnel diodes to rectify the antenna coupled IR radiation was in 2001 [1].

## 1.2 Infrared Energy Harvesting from Terrestrial Radiation

On the earth's surface, two large energy peaks can be observed across the electromagnetic spectrum. The first is in the visible range ( $\lambda = 0.5\mu m$ ), and is caused by the sun's radiation (the energy peak is often referred to as short-wave radiation). The other energy peak comes from the earth's own radiation, often referred to as terrestrial radiation or long-wave radiation. This energy peak sits around  $\lambda = 10\mu m$ , and is the target of our energy harvesting system. Using blackbody radiation physics, the size of the sun/earth, and distance separating the two, the total power incident (at 90 degrees) on the earth can be calculated as  $1377 W/m^2$ . As seen in Figure 1.3, only 51% of the energy is actually absorbed by the earth's

surface due to the atmosphere's absorption and reflection. The earth absorbs the energy from the sun (short-wave radiation), and brings itself into thermal equilibrium (since it has heated up) by reradiating energy at a longer wavelength (terrestrial or long-wave radiation). Figure 1.4 shows these two spectrums, and for wavelengths between  $7\mu m$  to  $13\mu m$ , the energy flux is about  $100 W/m^2$ . In order to actually transfer heat energy, the receiver (in our case the rectenna energy harvesting system) must be at a lower temperature than the radiation source (the earth). This would suggest the use of cooling mechanisms. However, certain environments (such as the desert where the air can be much cooler than the ground, or a plane flying high in the atmosphere) are capable of achieving this without external cooling components.

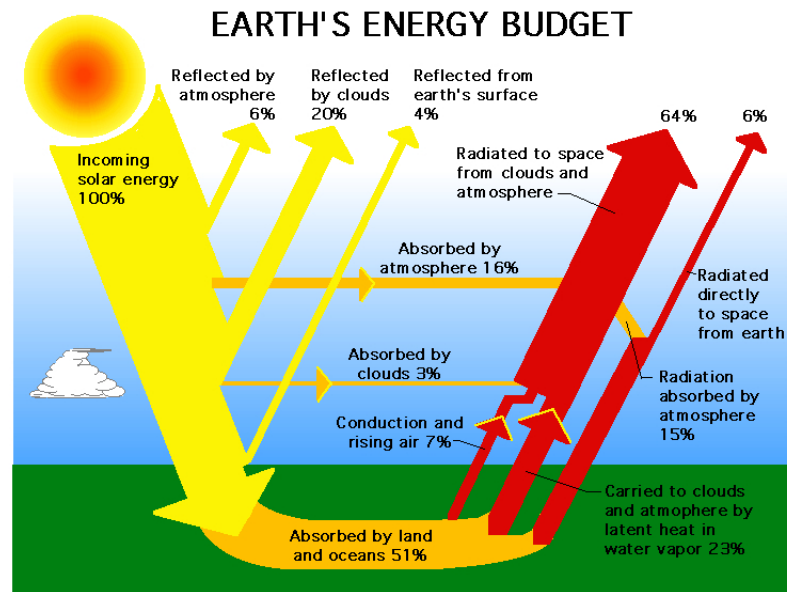


Figure 1.3: Solar radiation energy distribution at the Earth by Frank van Mierlo from <http://education.gsfc.nasa.gov>

It is desired to harvest energy from the long-wave infrared (LWIR) spectrum because its distribution on the earth's surface is more uniform with regards to lat-

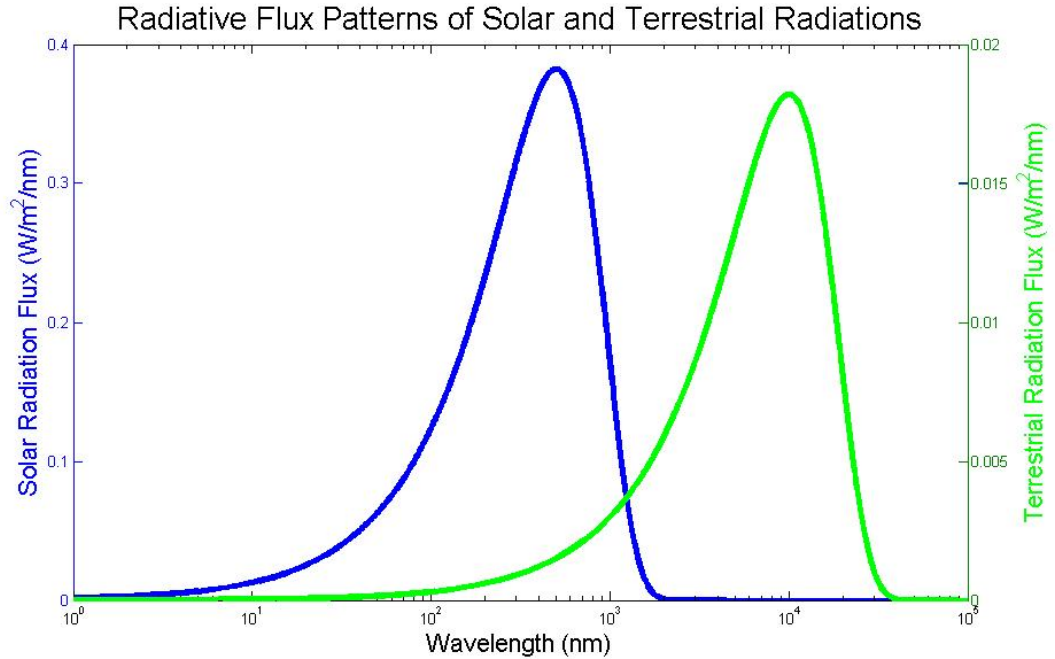


Figure 1.4: Solar and terrestrial radiation energy flux

itude. This is because long-wave radiation is essentially heat which can disperse itself about the earth's surface easily through ocean currents and air flow. Moreover, there is less of a variance between day and night radiation compared to the short-wave spectrum. Another advantage of LWIR is the relative lack of absorption in the atmosphere at the spectrum peak (wavelengths  $8\mu m$  to  $14\mu m$ ). For these reasons, LWIR makes a useful source of energy to harvest. Due to the particular wavelength of radiation, harvesting has been a challenge, with ACMIM diodes being one of the few devices capable of the task at a reasonable fabrication cost.

### 1.3 ACMIM Tunnel Diode Design Specifications

The antenna design must take into account the goals of 1) effectively coupling incident IR radiation from the ambient environment, 2) effectively coupling the AC signal to the MIM diode and 3) creating an acceptable MIM junction. These goals and processing techniques impose constraints upon the antenna design, namely geometry and material choice.

Using half-wave dipole antenna theory, the length (half) of the antenna in order to resonate at the desired LWIR band of frequencies (centered around 30  $THz$ ), should be  $5\mu m$ , well within modern lithography resolutions. To increase the total coupled power, a broadband antenna is highly desired to capture the wide continuum of LWIR frequencies, as well as a design that can utilize a wide polarization angle.

The MIM tunnel junction is formed by the metal portions of the antenna separated by a thin insulator film. When an AC signal is coupled across the junction, the potential energy of free electrons rises on one side compared to the other electrode. With enough energy, the electrons can tunnel through the very thin insulator film. The tunneling electrons represent a current, and any imbalances between the positive and negative cycles of the AC signal results in a net DC current flow, or in other words, rectification. The material and geometry choices here play a crucial role in determining current levels, as the the probability of electron tunneling is exponentially dependent on the barrier height (difference in Fermi level in the metal and insulator conduction band edge) and barrier width (insulator thickness).

Smaller barrier heights and thicknesses will each lead to exponential increases in current magnitudes.

In order for the MIM diode to actually rectify the coupled AC signal, it must respond faster than one wave cycle. With tunneling times for an electron through a  $2nm$  oxide quoted to be less than  $10^{-15}s$  [15, 8], this mechanism will not limit IR detection. The physical formation of the junction, however, can introduce cut-off frequency limitations due to the RC time constant. The junction resistance and capacitance are coupled to each other; decreasing the area leads to a smaller capacitance but larger resistance in the junction, and decreasing the oxide thickness increases capacitance but lowers resistance. The values of the junction resistance and capacitance are also important in matching the impedance of the antenna to ensure maximum power transfer.

As mentioned earlier, an asymmetry in the current-voltage relation about the bias point is required for rectification. Achieving this asymmetry can be done through bias (like the IR detector case) and material selection. If two different metals are chosen for the MIM junction, the work function difference can cause a built-in offset that leads to the current-voltage relation asymmetry. Certain materials, however, have high injection barriers that lead to larger junction resistance values [7]. To keep the resistance low (to reduce the frequency limitations caused by the RC time constant), identical materials should be used, and the asymmetry must be created through another method, such as geometry discussed in the next chapter.

The substrate upon which the ACMIM diodes are fabricated also plays an

important role in the performance. The particular material and thickness will affect the radiation coupling of the antenna, as well as processing feasibility. A standard silicon wafer topped with a native oxide film  $SiO_2$  is commonly used, and the insulating layer minimizes substrate leakage currents and capacitive coupling. The use of an insulating surface, however, introduces fabrication limitations because it can complicate and cause problems with the electron beam lithography, degrading resolution [27].

Minimum variation amongst fabricated devices is required for eventual array construction for energy harvesting systems, shown in Figure 1.5. The array design also will require mass fabrication using low-cost materials, over large spatial areas, typically involving a single or two layer metal deposition process.

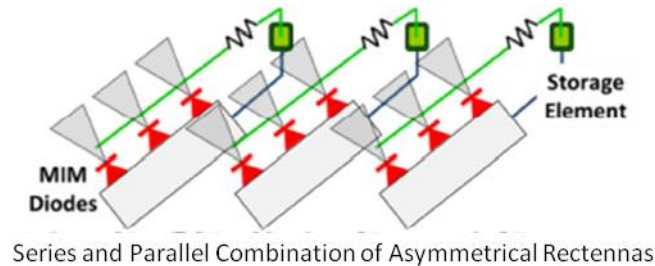


Figure 1.5: ACMIM array construction

Next, we summarize our design approach used to surmount the problems of frequency response limitations (due to resistance and capacitance of junction), asymmetric current-voltage relationship, and tunneling behavior through the following:

- Bow tie antennas are used for their broadband and polarization advantages
- Nickel is used as the antenna material because of its high frequency properties

and ability to fabricate a native oxide

- The use of a Ni/NiOx/Ni structure has a low injection barrier ( $0.2eV$ ) [10], thus lowering the junction resistance
- A geometrically asymmetric structure is used for the MIM diode by creating a sharp tip for one electrode and a flat edge for the other. This design also decouples the resistance and capacitance, improving the frequency response.

## 1.4 Thesis Contribution

This thesis discloses:

- A geometrically asymmetric bow tie antenna coupled Ni/NiOx/Ni MIM tunnel junction, designed for  $10\mu m$  wavelength IR detection.
- A “rectenna” structure capable of coupling ambient radiation into the tunnel junction that rectifies the signal.
- A decoupling of the MIM junction resistance from the parasitic capacitance by designing one of the electrodes as a sharp tip, and utilizing geometric field enhancement.
- A finite element method based multi-physics set of simulation results, used to optimize the antenna and the MIM junction geometry.
- A discussion of the possible existence of filaments across the insulator gap that are caused by “field forming” (electric field induced migration of metal), and

essentially act as shunt resistances.

- A detailed analysis of the shunt resistances' effect on rectification performance of ACMIM diodes.

## 1.5 Thesis Organization

The rest of the thesis is organized as follows: In Chapter two, physical phenomena behind the ACMIM diode operation are considered. In Chapter three, ACMIM diode radiation coupling performance and electrostatic operation is investigated through simulation results computed by a commercial finite element analysis software. Equivalent circuit models and simulation results showing the shunt are presented in Chapter four. And finally, in Chapter five, the thesis contribution is summarized and future project directions are discussed.

## Chapter 2

### Background

This chapter provides an overview of the ACMIM diode operation. Discussions include the basic tunneling mechanisms, the use of geometric asymmetry to provide current-voltage asymmetry, and bow tie antenna design. Also included in this chapter is a discussion on previous experimental results from fabricated devices.

#### 2.1 Tunneling Methods

From quantum mechanics, it can be shown that electron transition through a thin potential barrier is possible. In a MIM structure (band edge versus position diagram shown in Figure 2.1), a thin film of insulating material (thickness  $d$ ) sits between two conducting metals (assumed to be the same metal in that diagram). Due to the difference in work functions of the metal and insulator, a potential barrier of  $\phi$  is formed. Early research into tunneling conduction in MIM structures was done by Schottky, Millikan, Fowler, and Nordheim [5, 13, 22, 16], which addressed field, thermal, and photon assisted tunneling. Simmons lead the mathematical modeling of tunneling currents with his work in the 1960s [25, 26, 24]. Recent research has built off these contributions and introduced the study of trap assisted tunneling currents as well [18].

When a potential bias is applied to the MIM structure, the band edge versus

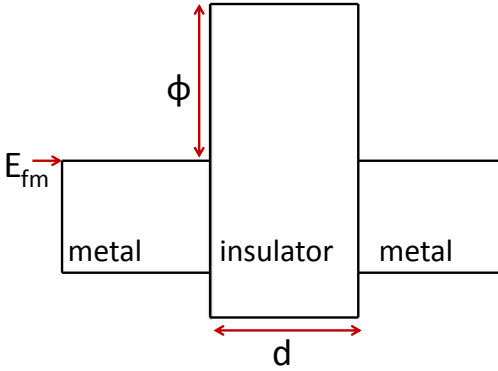


Figure 2.1: Energy band diagram of MIM tunnel diodes

position graph changes to show a higher energy for one of the metals, and a slanted energy level in the insulating layer. This general behavior can be seen in all the plots of Figure 2.2, where three different assist mechanisms for tunneling are presented. In plot “a”, field assisted tunneling behavior is shown. Most of the transport is due to electrons near the Fermi level of the metal, driven across the oxide because of the high fields. It should also be noted that the high fields causes the image charge effect where the potential barrier tip is rounded off. In the Fowler-Nordheim regime of field assisted tunneling, the band energy level is slanted so severely that an electron can see a thinner effective barrier (an electron is more probable to tunnel then, and “rolls” down the band edge to the other metal to complete the transition). In plot “b”, thermally assisted tunneling is shown. In this mechanism, electrons can have substantial thermal energy (electrons do not sit at the Fermi level) that could allow them to jump the barrier. In plot “c”, an incoming photon provides enough energy to an electron to move it to an energy level where tunneling is more probable.

Another tunneling mechanism involves defect trap levels in the insulating layer.

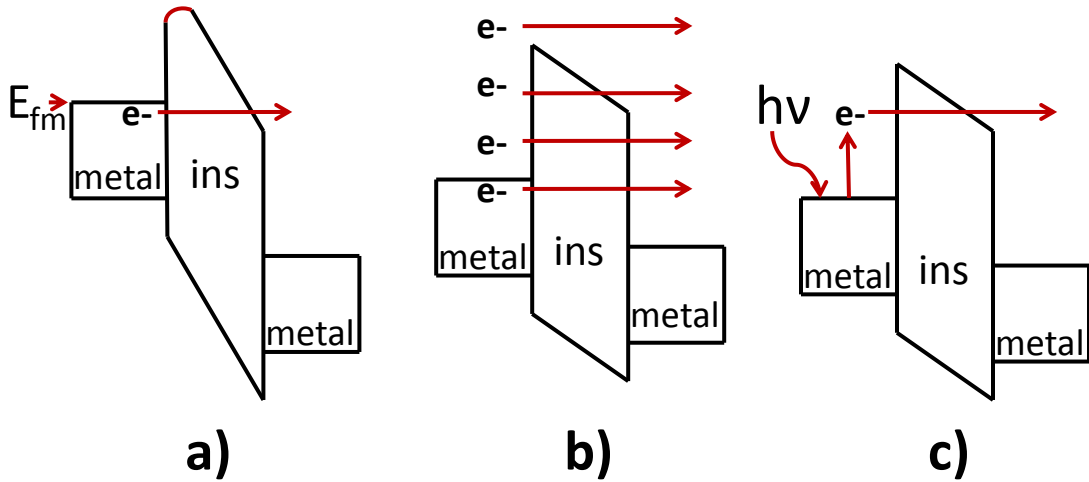


Figure 2.2: Tunneling mechanisms in MIM tunnel junctions: a) Field assisted b) Thermal assisted c) Photon assisted tunneling

Transitioning through thinner oxides is much more probable than through thicker oxides. With trap levels in a thicker oxide, however, tunneling can still occur. Multiple transitions make up the process: from metal to trap, then from trap to other metal. Each transition is over an effective oxide thickness that is smaller, resulting in higher probability of tunneling. However, this process can only occur if the trap is empty, somewhat limiting the actual tunneling current. Utilizing the Fowler-Nordheim regime or trap assisted tunneling both create an effective oxide thickness that is smaller. This allows the use of thicker and more robust oxides in design and fabrication, with the current levels and behavior of thinner insulating layers in the MIM structure.

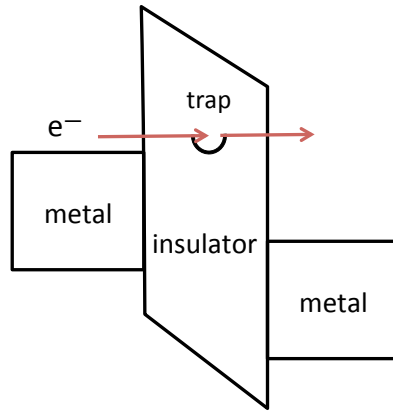


Figure 2.3: Trap assisted tunneling mechanism in MIM junctions

## 2.2 Geometric Field Enhancement

Using an asymmetric geometry has two main advantages for the rectenna application. First, the design decouples the resistance and capacitance of the junction that can allow better frequency response with a smaller RC time constant. The design also provides asymmetry in the current-voltage relation due to unbalanced electric field strengths in forward and reverse bias. The asymmetry in current-voltage relations is necessary for rectification, and can also come from the use of two metals (giving rise to a built-in shift in the energy bands, but also increasing the injection barrier height and thus resistance), or temperature differences (not suitable for energy harvesting applications due to external heat source). With these drawbacks, it is obvious that geometric asymmetry fits this application the best.

In Figure 2.4, the geometrically asymmetric design is shown with one electrode flat and square like, with the other electrode pointed and triangle like. With an applied bias across the two electrodes, the energy bands will shift as they did

in the tunneling discussion. Due to the geometric asymmetry, the electric field will be much stronger at the tip of the pointed electrode due to the lightning rod effect. This high electric field can cause substantial tunneling currents to flow (field assisted tunneling and Fowler-Nordheim regime). When bias is applied with opposite polarity, the bands once again shift, but the resulting field assisted tunneling current will be smaller due to the much weaker electric field at the flat edge electrode (lack of lightning rod effect). Using geometric asymmetry to provide asymmetry in current-voltage relations for a MIM diode has been theoretically proven [14] and experimentally shown [3, 2].

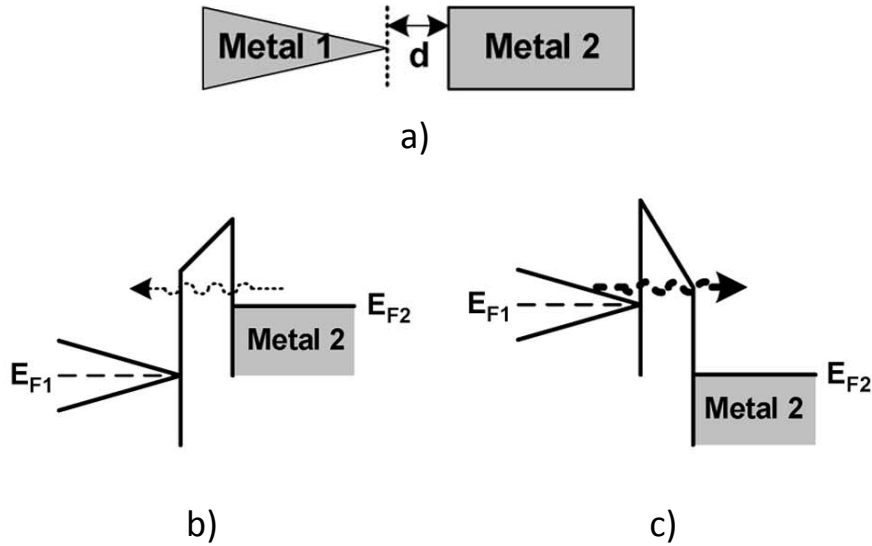


Figure 2.4: Geometrically asymmetric MIM diode: a) physical structure b) low field tunneling current c) high field tunneling current (adapted from [3])

In Figure 2.4, the energy band slant in the oxide region is assumed to be linear, but in reality, the energy band in the oxide is non-linear (shown through

simulations in Chapter 3), giving rise to a band structure seen in Figure 2.5. The potential across the gap does not vary linearly, but decays rapidly near the tip of the pointed electrode, and more slowly near the flat edged electrode. In reverse bias, the potential diagram looks like plot “b” and the barrier thickness for tunneling is much wider than that of the forward bias case (plot “c”). With different potential barrier thicknesses, the quantum mechanical probability of tunneling is different, giving rise to an imbalance in current magnitudes when the diode is biased with opposite polarities, or rectification ability.

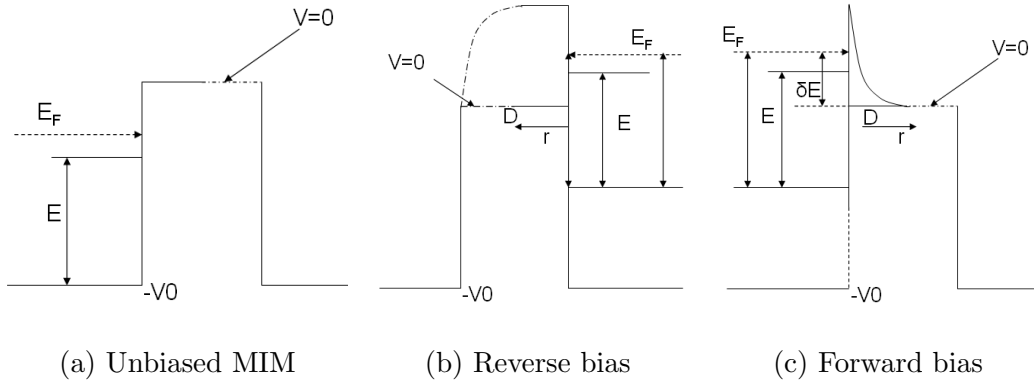


Figure 2.5: Asymmetric geometry induced rectification illustration on the potential energy band diagrams (from [23])

One of the main limiting factors of MIM operation at high frequency is the response of the junction’s resistance and capacitance. In typical junctions, the resistance  $R$  and capacitance  $C$  are coupled through the area  $A$ , as shown in Equation 2.1 (capacitance is proportional, while the resistance is inversely related).

$$C = \epsilon \frac{A}{d} \quad \text{and} \quad R = \frac{dV}{dI} = \frac{dV}{AdJ} \quad (2.1)$$

In the asymmetric planar structure though, the current flow is not as heavily dependent on area as it is on the tip sharpness. With a sharp tip, the current is more heavily focused into a smaller area, reducing the resistance and capacitance. This decoupling allows the manipulation of the RC time constant through sizing of the junction, which can be reduced to allow higher frequency operation.

### 2.3 Antenna Design

To capture incoming IR radiation ( $\lambda = 10\mu m$ ) and couple it to a circuit (in our case the demodulation diode), a simple planar antenna is needed. As ambient AC radiation interacts with the antenna structure, surface currents are induced in the metal antenna, which are then applied to an external circuit. In an integrated rectenna structure, the induced oscillating currents are funneled down the antenna to the rectification element (diode), all within the same device.

Material choice for the antenna can affect performance if the chosen material is too lossy. At terahertz frequencies, some materials can start to behave as an imperfect conductor, introducing power losses that affect overall energy harvesting efficiency. Nickel is typically used in ACMIM design at the frequencies we are interested in because it is practically lossless (and IR is below its plasmon frequency). Other metals may have this property, but were not suitable for the MIM diode portion of the device. The nickel and nickel oxide combination gives a low injection barrier (about  $0.2eV$  [9]) that other materials could not achieve (or fabricate easily).

Bow tie antennas, while closely related in operation and design to standard

dipole antennas, offer some unique advantages that make them suitable for the IR energy harvesting application. The resonant frequency of the antenna is related to the length of a side of the antenna. For 30  $THz$  IR radiation, a single side of a half-wave dipole antenna would be  $2.5\mu m$ . This antenna design offers good power coupling at the exact center of the device (where the MIM junction would be), and the voltage and current distributions across the antenna length can be seen in Figure 2.6. Based on the flare angle of the bow tie antenna, the bandwidth of the antenna can be increased in comparison to the simple dipole antenna [6]. This is an important property because the IR radiation attempting to be harvested lies in a broad spectrum. Having a broadband antenna allows more power to be harvested from these other wavelengths in the ambient environment. Dipole antennas also have stricter polarization requirements. The flare angle allows radiation at different polarization angles (unpolarized waves are typical in the ambient environment) to be coupled in and thus more power can be applied to the diode for rectification. The final, and most important, design characteristic of the bow tie antenna is its ability to focus the energy in a very small (nanometer) area, providing small junction resistance and capacitance needed for rectification at such high frequencies as IR.

While it is necessary to keep the bow tie structure symmetrical for optimal power coupling performance, the junction itself can locally be made geometrically asymmetric in order to achieve the desired current-voltage relationship asymmetry. One side of the bow tie is left unchanged (i.e. a sharp pointed tip), whereas the other side is modified at the middle (where the MIM junction would be) to have a flat edge square like component. This novel approach balances the need for a sym-

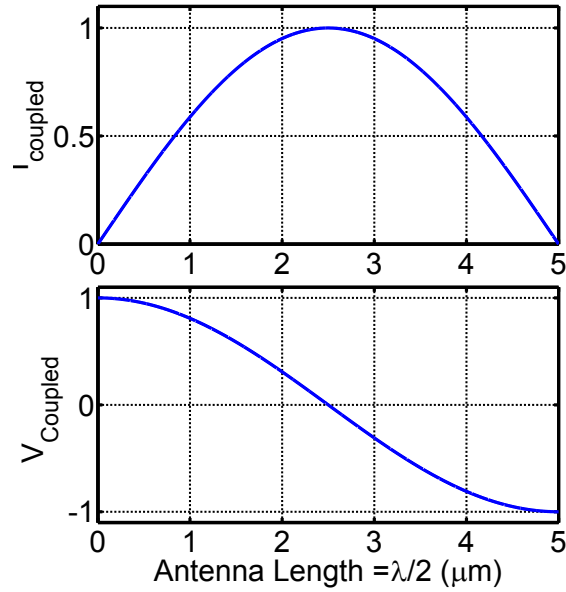


Figure 2.6: Normalized voltage and current distributions on a half-wave dipole antenna

metric antenna structure with the necessary geometric asymmetry for rectification purposes. The structure can be seen in the current density plots presented in Figure 2.7. These plots were generated using finite element analysis software (see chapter 3 for simulation details), and model the surface currents for excitation by a polarized  $30 \text{ THz}$  IR wave.

In the left plot of Figure 2.7, power funneling can be seen on both sides of the antenna. The surface current density increases in strength as you move from the outer portions of the antenna to the narrower regions near the MIM junction in the center. In both plots, (particularly the right), the current appears to be highly concentrated to the tip of the pointed electrode, at an amplitude of  $1.4 \times 10^7 \text{ A}$  (incident power density of  $2.7 \times 10^{-3} \text{ W}/\text{m}^2$ ). These plots confirm that the current

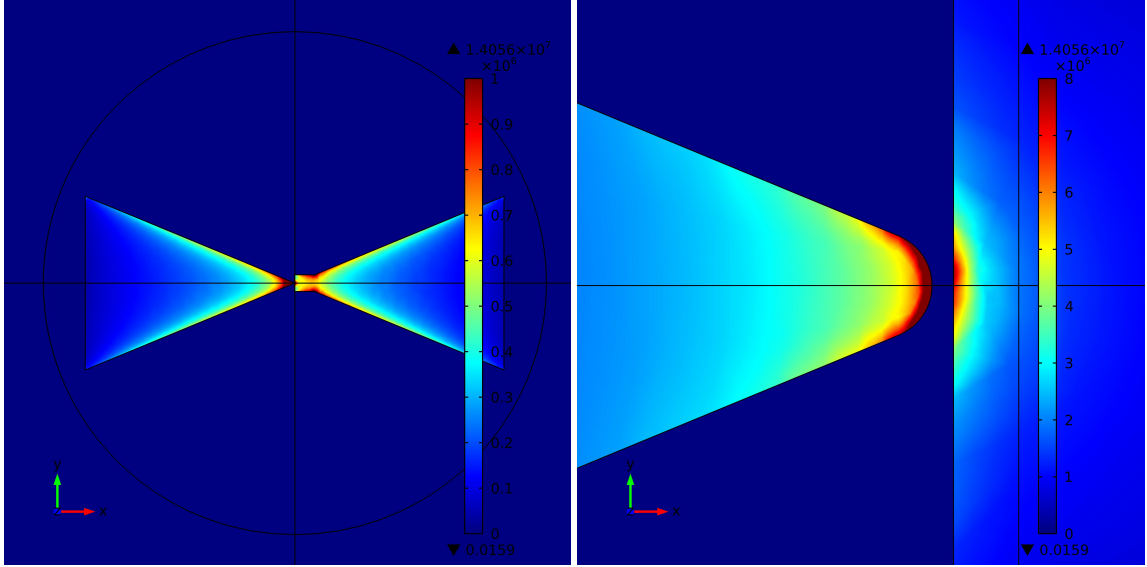


Figure 2.7: Surface current density density of antenna (left), zoomed view at the junction (right). Color scale left: red ( $1 \times 10^6 A$ ) to blue ( $0A$ ). Color scale right: red ( $8 \times 10^6 A$ ) to blue ( $0A$ )

is highly focused in a small area, justifying the decoupling of junction resistance and capacitance assertions made earlier.

$$\delta = \sqrt{\frac{2\rho}{2\pi f\mu}} \quad (2.2)$$

Equation 2.2 can be used to calculate the skin depth, or the region where most of the (surface) current flow is concentrated within the metal's thickness. Using a frequency of  $30THz$ , a thin-film resistivity  $\rho$  of  $9.7\mu\Omega.cm$  [21], and a relative magnetic permeability of 1 (due to the high frequency [12]), the skin depth is calculated to be approximately  $25nm$ .

## 2.4 Previous Fabrication and Experimental Results

The devices analyzed in this work were fabricated by Yesilkoy *et al.* [27]. Detailed processing and testing techniques are disclosed in this reference. During the testing of fabricated devices, a parameter analyzer sweeps and measures a current-voltage relation. A plot is shown in Figure 2.8 for a typical device. These devices responded moderately well to incoming radiation from a laser during testing. The devices are then taken from the testing apparatus and then put back on the parameter analyzer, when the subsequent current-voltage relationship plot no longer looks nonlinear as it did previously, but practically linear. These now linear devices respond even better, and show more rectified DC power. This result should not happen theoretically: linear devices do not possess the mismatch in current magnitudes necessary for rectification to occur.

The cause of the linearization of the device's current versus voltage curve results from electrical stress, either from testing (radiation, parameter analyzer) or electrostatic discharge (ESD). With high enough electric fields in the insulator region of the MIM structure, the metal begins to migrate and can form very thin filaments from one side of the junction to the other. These filaments essentially act as shunts of a given resistance, and provide another current path in addition to the tunneling path that holds the rectification properties.

The goal of Chapter four of this thesis is to analyze the equivalent circuit models of the ACMIM device, and to introduce a small shunt impedance across the diode in an attempt to understand why rectification performance has increased with

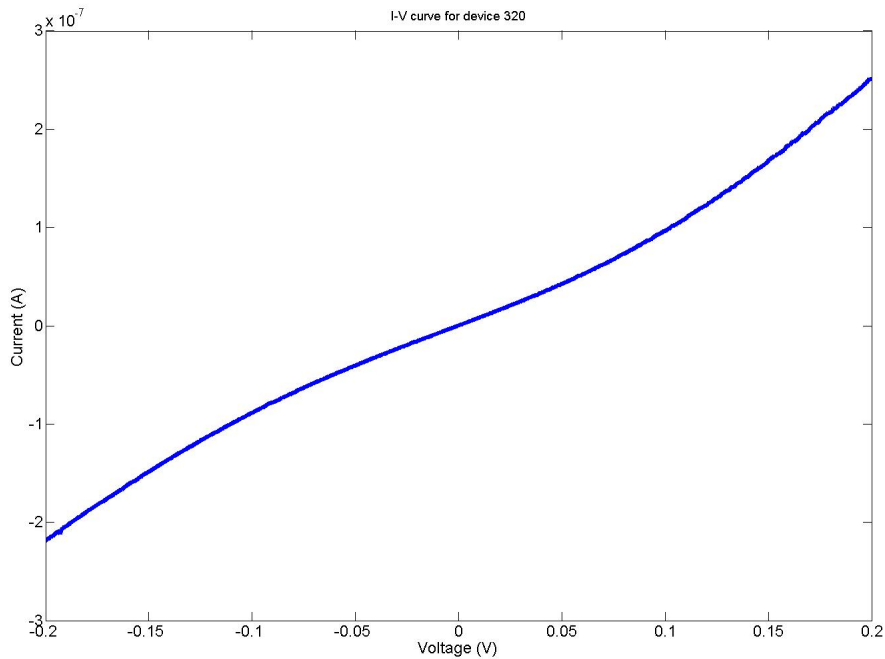


Figure 2.8: Current versus voltage plot for a typical fabricated ACMIM diode

the apparent linearization of the device.

## 2.5 Summary

- Tunneling mechanisms in MIM structures were described in detail.
- Geometrically asymmetric structures and the resulting field enhancement technique provides an asymmetric current-voltage relationship.
- The geometrically asymmetric approach also allows for the decoupling of the junction resistance and capacitance.
- An improvement in frequency response resulting from this decoupling is further demonstrated.

- Bow tie antenna design, operation, and advantages were presented and optimized for 30  $THz$  IR radiation.
- Experimental data from previously fabricated devices was presented, with a discussion of the testing results.

## Chapter 3

### Finite Element Simulation Results

In order to optimize the ACMIM design from an electrostatic and electro-dynamics point of view, various material and geometric parameters were adjusted and simulated utilizing COMSOL Multiphysics, a commercially available Finite Element Analysis (FEA) based software.

#### 3.1 Electrostatic Simulation Results

To simplify the electrostatics analysis of the ACMIM diode structure, the rectenna was modeled as a single plane structure, with a small air gap between the triangle and square segments, shown in Figure 3.1. To setup the simulations, a DC voltage of  $1V$  was applied to the triangle electrode, while the square side was grounded at  $0V$ . The electric field as a function of distance across the gap was plotted, and the maximum value recorded, referred to as “E-field Norm”. By analyzing the shape of the electric field versus distance plot and its maximum/minimum values, the full effects of the geometric changes can be understood.

Some important geometric parameters used in this study are as follows:

$L$  : Length of the triangle and dimension of the square

$r$  : Radius of curvature of the tip

$\theta$  : Flare/bow angle of the antenna

$d$  : Gap width between the triangle and the square

$t$  : Metal film thickness

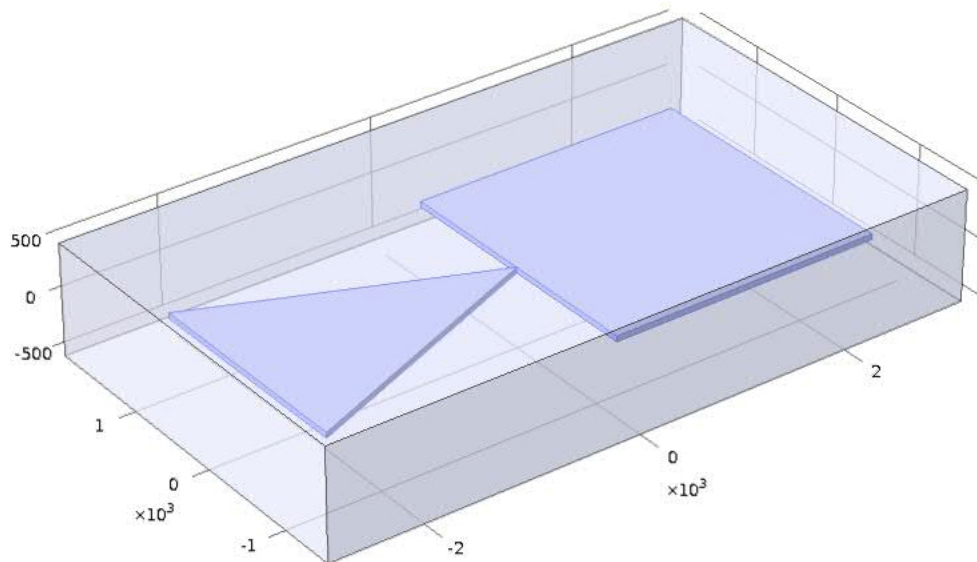


Figure 3.1: Geometric model used in the majority of the simulations. Dimension units are in  $nm$

### 3.1.1 Mesh Density Analysis

The general principle behind FEA involves dividing a particular geometry into many discrete small volumes (collectively called a mesh), and numerically solving the equations governing the particular physics the user is interested in, using adjacent elements as boundary conditions and assuming the solution in a particular discrete

volume element is constant. Multiple iterations may be necessary to converge on an overall solution, especially if the model is not divided into a sufficiently dense mesh.

To ensure valid and realistic results for a particular geometry, a mesh density analysis must be performed initially. Starting with a larger element size in the mesh and incrementally reducing the size, the values for a particular metric should converge. The idea is to pick a mesh sizing that gives that converged solution, but requires the minimal amount of elements in order to save processing time and computing power. The geometry chosen for this analysis was:  $L = 2.5\mu m$ ,  $\theta = 45$ ,  $r = 5nm$ ,  $t = 50nm$ ,  $d = 10nm$ , and the metric used for comparison amongst trials was the maximum electric field along a plane that slices the structure in the middle (at half the thickness of the metal).

COMSOL has built-in mesh parameter combinations (normal, fine, finer, extra fine, extremely fine) that are first tried, and the user has the ability to make custom meshes that tighten up the built-in combinations. Each subsequent mesh increases the number of overall elements, and as seen in Figure 3.2, eventually converges starting with the built-in “Extremely Fine” mesh profile.

The custom built mesh used for all further analyses has approximately  $2.6 \times 10^6$  discrete elements, and can be seen at various zoom levels in Figure 3.3. The entire structure is enclosed in a larger air box domain that is loosely meshed, and a smaller air box domain near the junction (much more finely meshed, since this is where the results we are interested in are located). Within the smaller air box, the metal near the junction can be discretized with much smaller elements as well. This allows more accurate results in this area, while not increasing the computation time significantly.

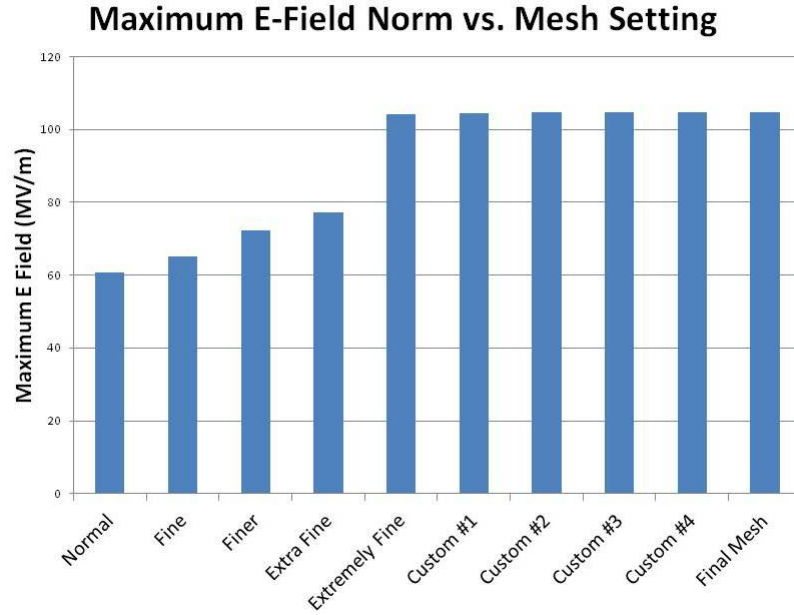
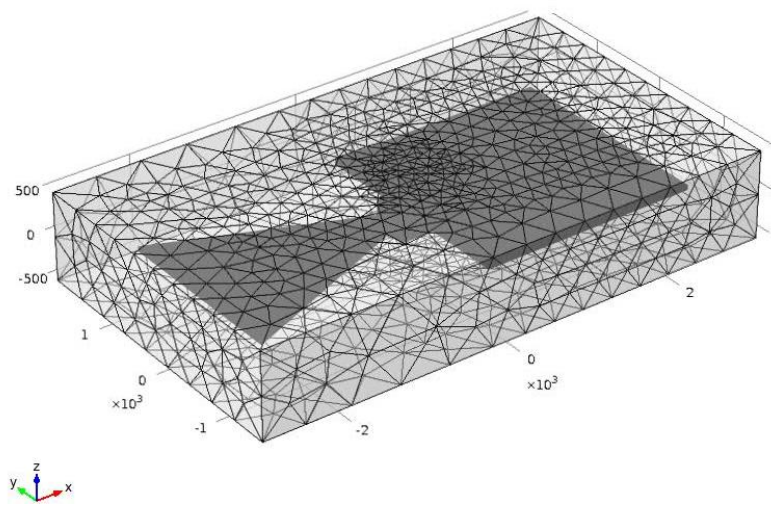


Figure 3.2: Maximum E-field magnitude values computed at various mesh profiles

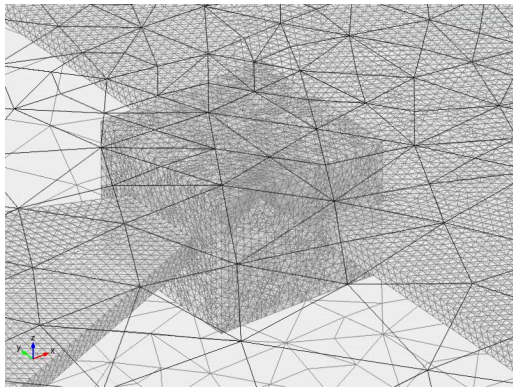
### 3.1.2 Tip Radius Analysis

For good geometric field enhancement, the ACMIM design must have a sharp tip, with minimal radius of curvature. The sharper tip concentrates the current flow to a smaller area due to the electric field enhancement. This behavior minimizes the junction capacitance while decoupling the junction resistance and keeping it small. Since the sharp tip is only on one side of the junction, the electric field is only enhanced on one side, generating an imbalance that results in asymmetric current flow and rectification.

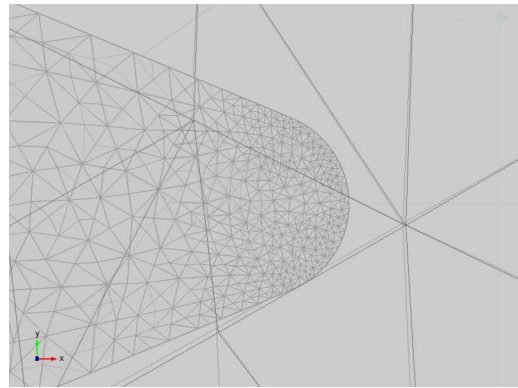
Due to processing constraints (lithography resolutions), the minimum achievable tip radius is limited. When electron beam lithography (EBL) is used along with the proximity effect correction, the highest available resolution is consistently achieved, and the minimum tip radius becomes more a function of metal grain size



(a) Whole simulation domain.



(b) Finer mesh box at the junction.



(c) Finer mesh at the tip.

Figure 3.3: Mesh profile used for FEA

and other thin film inhomogeneities. This gives rise to variation amongst devices that can drastically affect performance. In Figure 3.4, two devices under identical processing conditions produced a  $10nm$  tip radius-of-curvature and the other  $3nm$ .

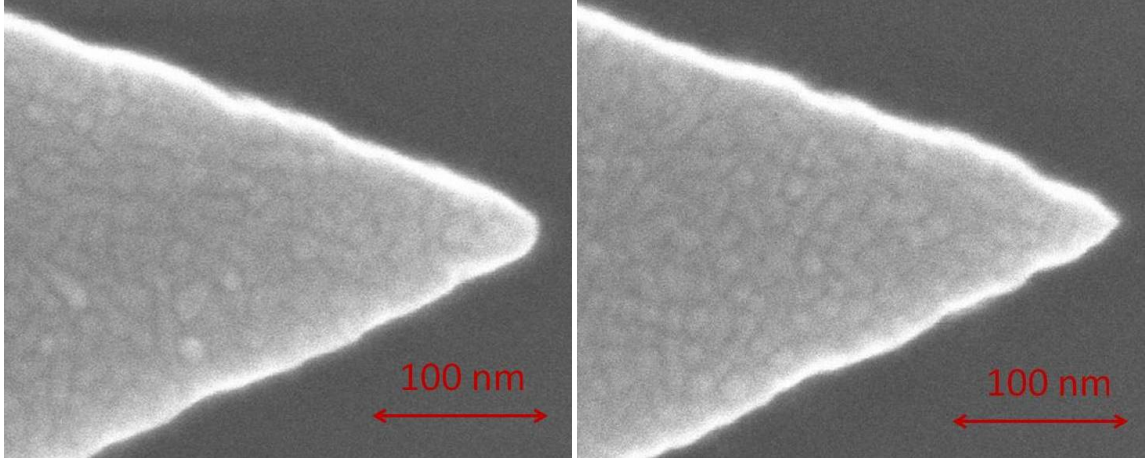


Figure 3.4: Micrographs of two tips with  $10nm$  (left) and  $3nm$  (right) radius of curvatures

Tip radius is also highly dependent on the chosen flare angle. In Figure 3.5, two tips with  $45^\circ$  and  $90^\circ$  flare angles with corresponding tip radius measurements are presented. This behavior is also summarized in the plot of antenna flare angle vs. tip radius of curvature. From this plot, it can be surmised that angles less than  $45^\circ$  have very limited effect on the minimum tip radius achievable, but at larger angles, the minimum achievable radius increases, where it is dependent on the metal grain structure.

To test the effect of changing the tip radius, a parametric sweep was run for radius values of  $3nm$  to  $10nm$  in  $1nm$  steps, while keeping the rest of the geometric parameters constant ( $L = 2.5\mu m, \theta = 45, t = 50nm, d = 2nm$ ). In Figure 3.6, two dimensional plots of the electric field magnitude distribution as a result of the  $1V$

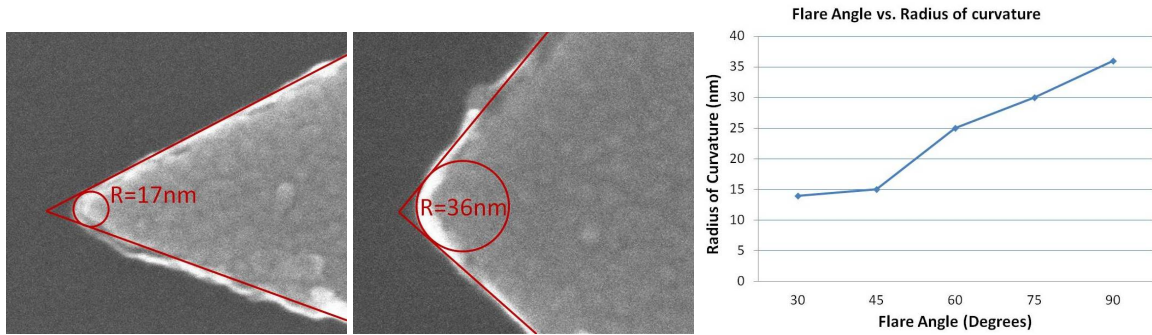


Figure 3.5: Radius of curvature of the tips with  $45^\circ$  (left) and  $90^\circ$  (middle) flare angles. Antenna flare angle vs. tip radius of curvature plot (right)

applied potential are shown. The color scale (red being the highest and blue lowest field) represents the effect of tip sharpness on the E-field enhancement. The electric field is highest and more concentrated at the tip and spreads out moving across the gap. In comparison of the two tips, the  $3\text{nm}$  radius has a larger maximum field ( $6 \times 10^8\text{V/m}$ ) than the  $10\text{nm}$  radius tip ( $5.3 \times 10^8\text{V/m}$ ).

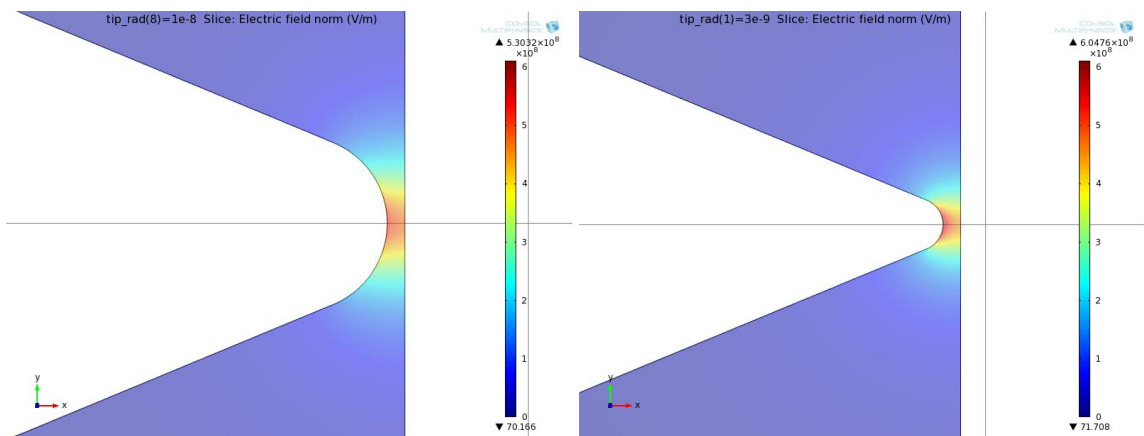


Figure 3.6: E-field norm surface plots with tip radius-of-curvature  $10\text{nm}$  (left) and  $3\text{nm}$  (right)

A line plot of electric field distribution across the gap for the different tip radius parameters is shown in Figure 3.7. The label “Arc length” along the x-axis is

an artifact from the parametric sweep setup and just denotes the overall macro-scale position. Each line is for a particular tip radius, and it only has values over a  $2nm$  gap span (they are shifted due to the way the geometric changes were implemented). The main takeaway from this plot is the high non-linearity in all the distributions (regardless of tip radius). For a geometrically symmetric MIM junction, the electric field across the gap would be uniform, whereas in this case for a sharp tip with geometric asymmetry, the electric field peaks right at the tip and decays non-linearly to the square electrode. Depending on where the electron current is extracted from (triangle tip or square flat edge), there will be an asymmetry due to the imbalance in electric fields (tunneling current depends on electric field). Also, the peak maximum and minimum values for electric field of each tip radius diverges as the tip radius gets smaller, as shown in Figure 3.8. Since tunneling current depends on the electric field, we can expect a smaller tip radius to yield larger current imbalances for positive and negative biases.

### 3.1.3 Gap Width Analysis

As mentioned earlier, the gap between electrodes (oxide thickness) is an important parameter affecting the MIM diode performance. A parametric sweep of the gap width from  $1nm$  to  $10nm$  in  $1nm$  increments, and then from  $10nm$  to  $25nm$  in  $5nm$  increments was performed. The electric field magnitude as a function of gap width is shown in Figure 3.9. Based off the fitted decay rates (maximum field decays at a rate of  $x^{-0.78}$  compared to  $1/x$  for the minimum electric field), it can

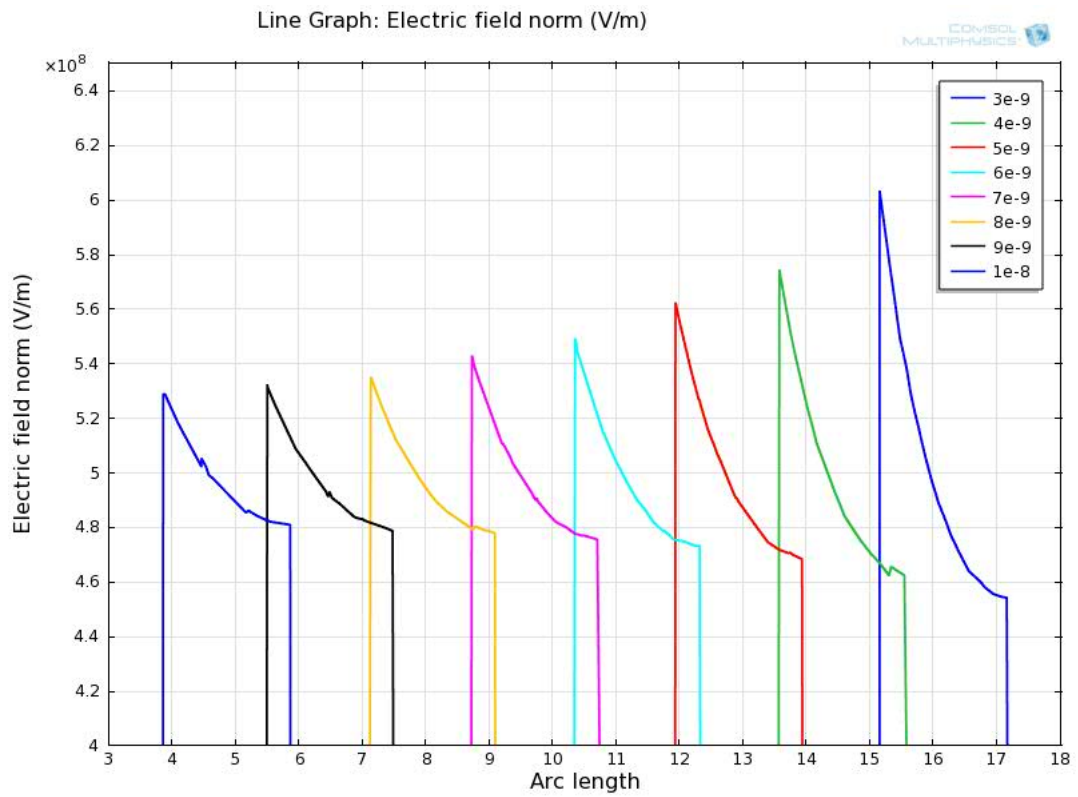


Figure 3.7: E-field norm line graphs at the  $2nm$  gap with tip radius  $3nm$  to  $10nm$

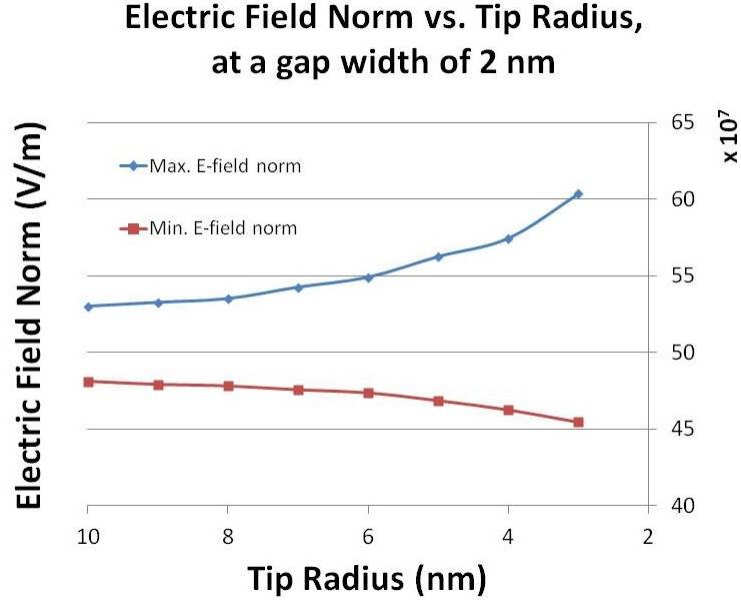


Figure 3.8: Max and Min E-field norms observed at the  $2nm$  gap as a function of tip radius

be shown that the asymmetric geometry effect decreases at larger gap widths. Two dimensional plots of the electric field magnitude distribution for gap widths of  $7nm$ ,  $10nm$ , and  $25nm$  are presented in Figure 3.10 (shown on the same color scale). Line plots of the electric field distribution across the gap are shown in Figure 3.11.

### 3.1.4 Flare Angle Analysis

The antenna design allows us to choose a flare angle of the bow tie, but this becomes a tradeoff between the bandwidth and electric field enhancement effects simulated here. Once again, a parametric sweep of the flare angle while keeping the other geometric parameters constant ( $L = 2.5\mu m$ ,  $r = 5nm$ ,  $d = 2nm$ ,  $t = 50nm$ ) was performed. The angle  $\theta$  was varied from from  $30^\circ$  degrees to  $180^\circ$  degrees

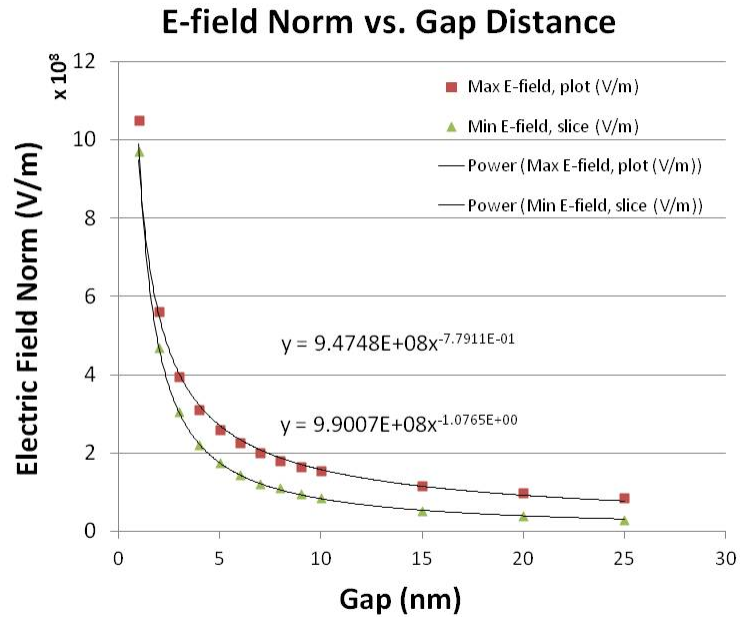


Figure 3.9: Max and Min E-field norm observed across the junction versus gap width

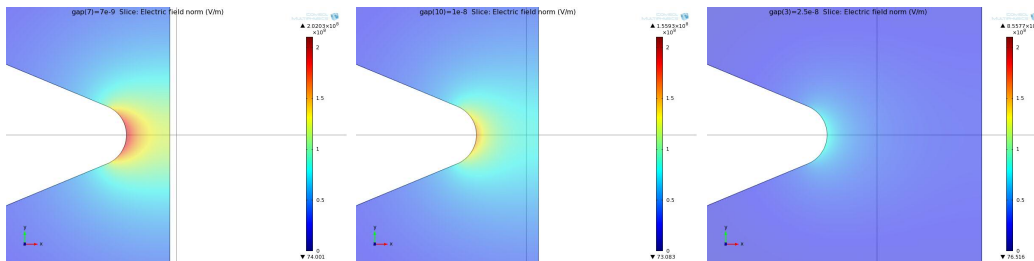


Figure 3.10: E-field norm surface plots with gap width  $7nm$  (left),  $10nm$  (middle) and  $25nm$  (right)

(equivalent to parallel plates) in  $15^\circ$  degree increments. Figure 3.12 shows the minimum and maximum magnitudes of the electric fields in the gap as a function of flare angle. This plot shows that the electric field across the gap is hardly influenced by the bow tie flare angle for values less than  $120^\circ$  (the tip radius and gap width effects dominate here). At large flare angles ( $\geq 120^\circ$ ), the maximum and minimum

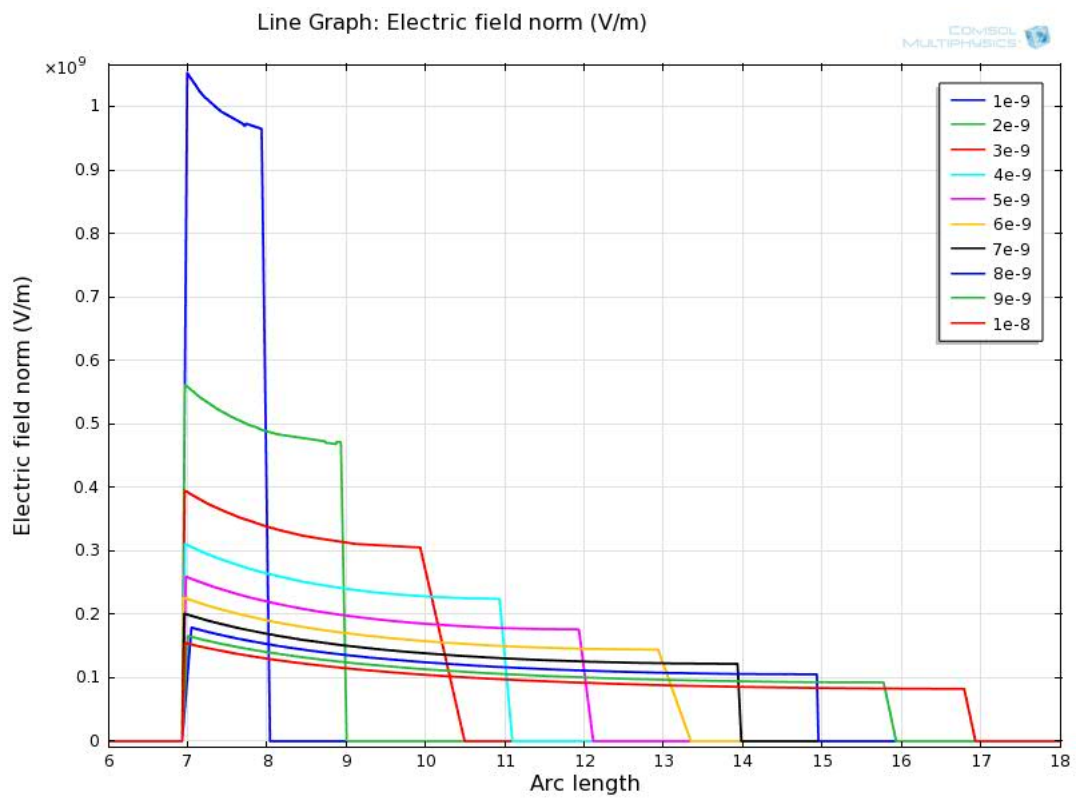


Figure 3.11: E-field norm line graphs with gap widths between  $1nm$  to  $10nm$

electric field values start to approach one another, showing a more constant field typical of a parallel plate configuration. In Figure 3.13 shows the two dimensional electric field distribution for flare angles of  $30^\circ$  and  $150^\circ$ . Although the field is still concentrated at the tip, larger flare angles will widen the area over which a substantial electric field is present, with smaller magnitudes as well.

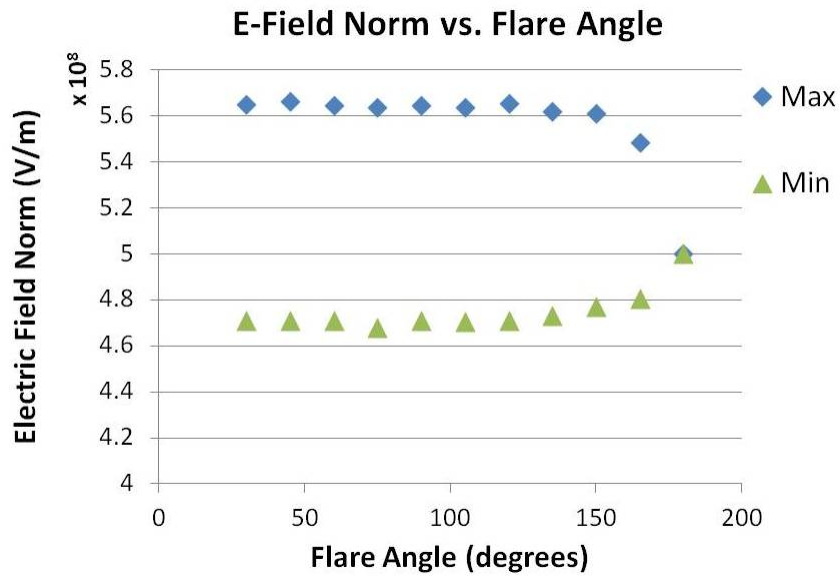


Figure 3.12: Max and Min E-field norms at the gap with changing flare angle

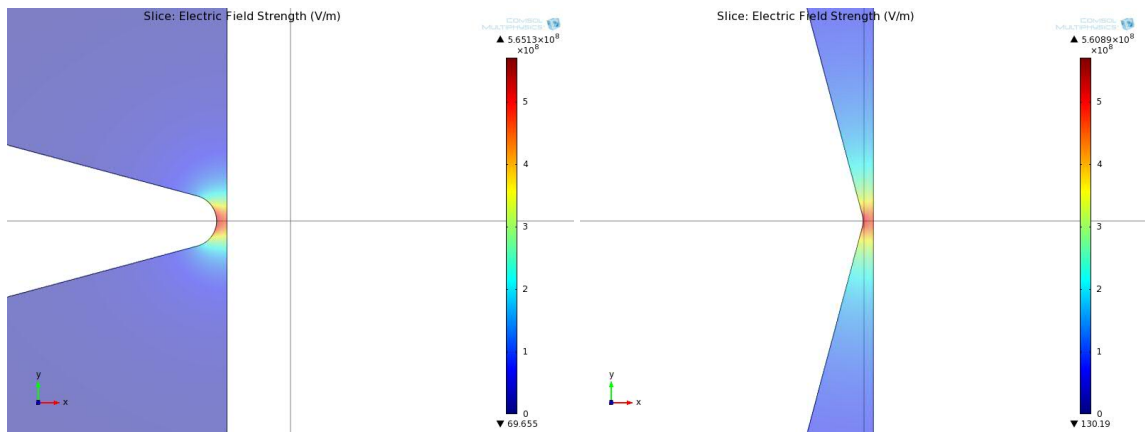


Figure 3.13: E-field norm surface plots with flare angles  $30^\circ$  (left) and  $150^\circ$  (right)

### 3.1.5 Capacitance Analysis

The capacitance of the junction of the MIM structure is very important to the operation of the overall device because it determines the RC time constant of the junction which influences the speed of the device. Each of the parameters changed in the previous simulations affects the geometry of the device and hence can alter the capacitance. Using COMSOL's built-in capacitance measurement module, the tip radius, gap width, and flare angle analyses are repeated, and a calculated capacitance is outputted. This value is calculated internally by a concurrent voltage sweep and measuring the terminal charge, giving  $(dQ/dV)$ .

In Figure 3.14, the results of the tip radius study are presented. The fitted function suggests a linear relation with larger capacitances corresponding to larger radiuses. This intuitively makes sense because capacitance is related to area, and a larger tip radius gives more tip area near the flat square electrode. According to this numerical estimation, for a geometry with  $r = 3nm$ ,  $\theta = 45^\circ$  and  $d = 2nm$ , the junction capacitance equals  $C = 3.1509 \times 10^{-17}F$ .

In Figure 3.15, the results of the gap width study are presented. The fitted function suggests that geometric asymmetric MIM diodes weakly depend on gap width with a decaying factor of  $x^{-0.05}$ . Equation 3.1 can explain why we see this weak dependence while in a parallel plate capacitor we get an inverse relation. This is because the electric field is  $V/d$  in a parallel plate capacitor, while in our case with the geometric asymmetry, the electric field is greatly enhanced and much larger than the simple  $V/d$  relation. As the gap width  $d$  decreases (should give

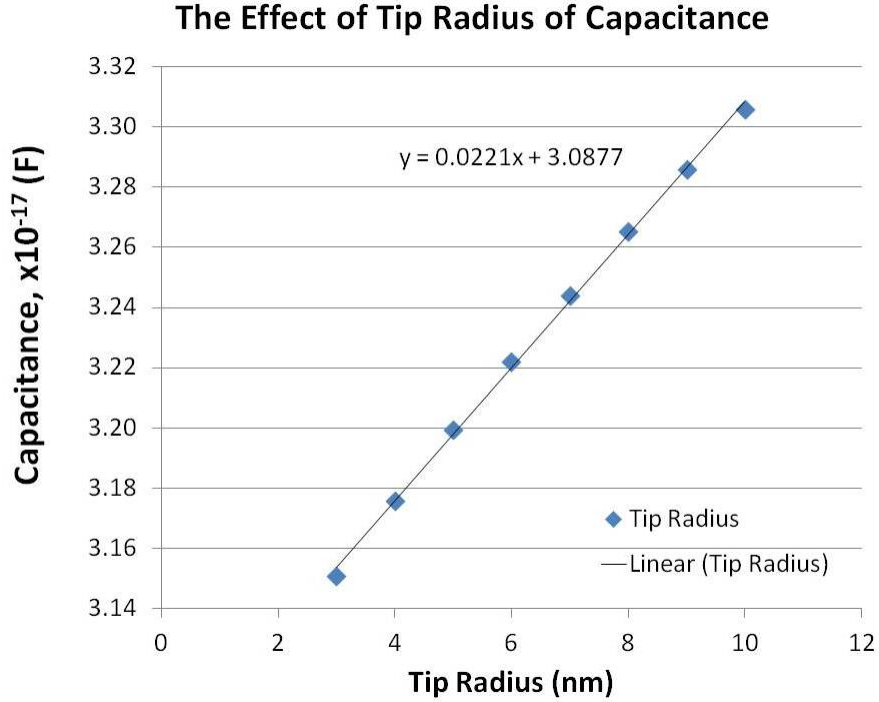


Figure 3.14: Junction capacitance vs. tip radius plot

larger capacitance), the electric field increases much more (in comparison to the parallel plate) giving a smaller capacitance. This partially offsets the  $1/d$  relation and results in a weaker dependence on gap width.

$$C = \frac{Q}{V} = \frac{Q}{Ed} \quad (3.1)$$

In Figure 3.16, the results of the flare angle analysis are presented. The fitted curve is fairly linear up until an angle of  $120^\circ$  where the capacitance increases rapidly. As the flare angle increases, more tip area is close to the square electrode, contributing to the capacitance. At larger flare angles ( $\geq 120^\circ$ ), the geometry starts to approach a parallel plate capacitor with a very large area (in comparison to the sharp/narrow tip case).

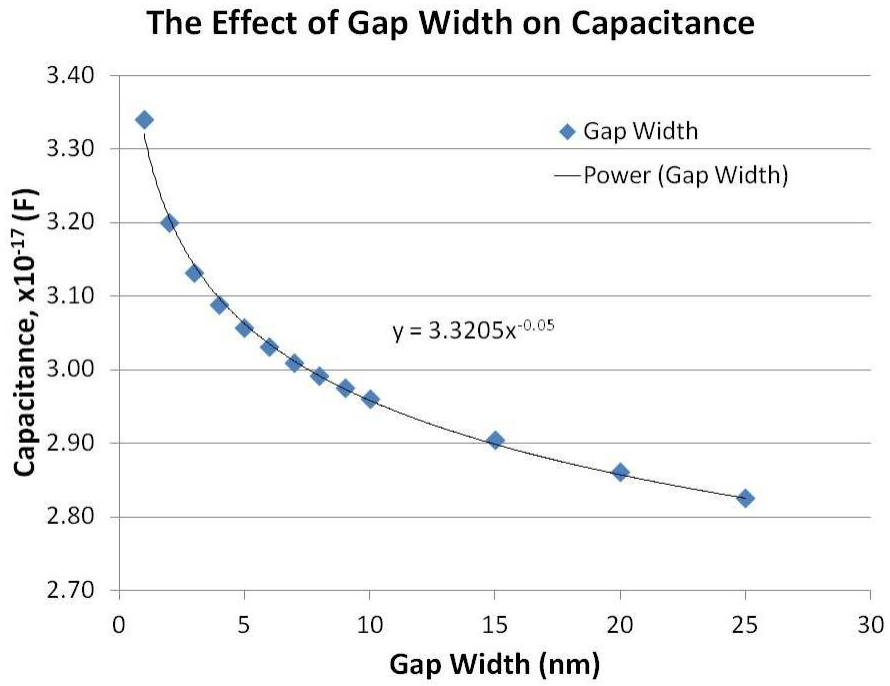


Figure 3.15: Junction capacitance vs. gap width plot

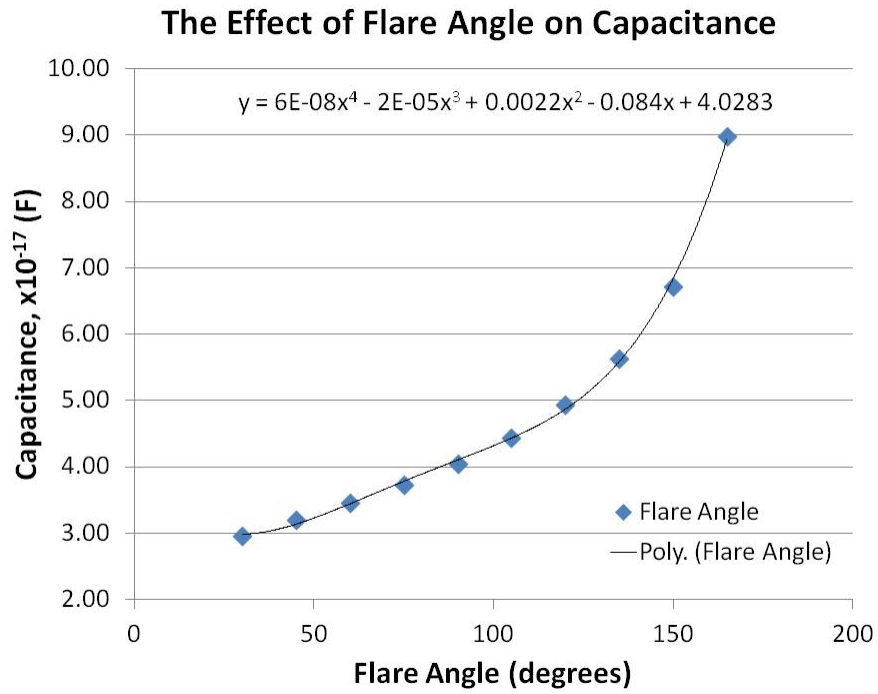


Figure 3.16: Junction capacitance vs. flare angle plot

### 3.1.6 Imperfection Effects

Due to slight fabrication variability and material properties (particularly grain structure), the tip commonly has many imperfections. In Figure 3.17, a typical tip with defects is shown. As can be imagined, these defects, if located near the tip, can drastically influence the operation. To study the imperfection's effects, circles of radius  $1nm$  and  $2nm$ , with their centers located on the tip line, are added to the geometric model in various configurations. As a baseline, the geometry without imperfections ( $r = 10nm$ ,  $\theta = 45^\circ$ ,  $d = 2nm$ ) gives a maximum electric field magnitude of  $5.33 \times 10^8 V/m$  and a numerically approximated capacitance of  $3.3 \times 10^{-17} F$ .

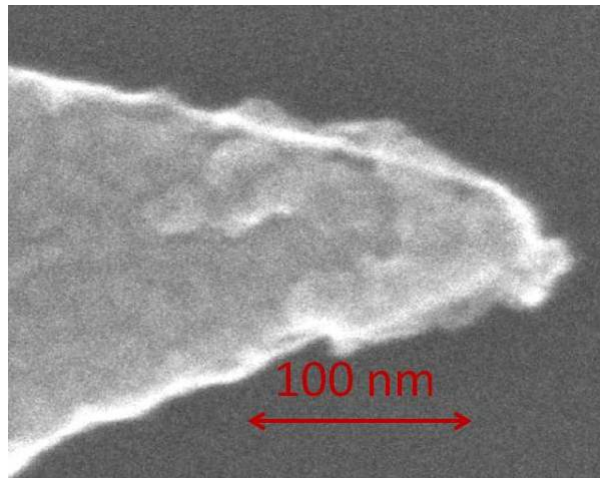


Figure 3.17: Micrograph of a defective junction tip

As clearly shown in Figure 3.18, these imperfections create hot spots that can further increase the electric field locally. The effects on the electric field are highly dependent on the imperfection's location and shape. Those near the very tip that actually decrease the distance to the flat electrode drastically increase the local electric field magnitude, as can be expected from the gap width analysis. Also,

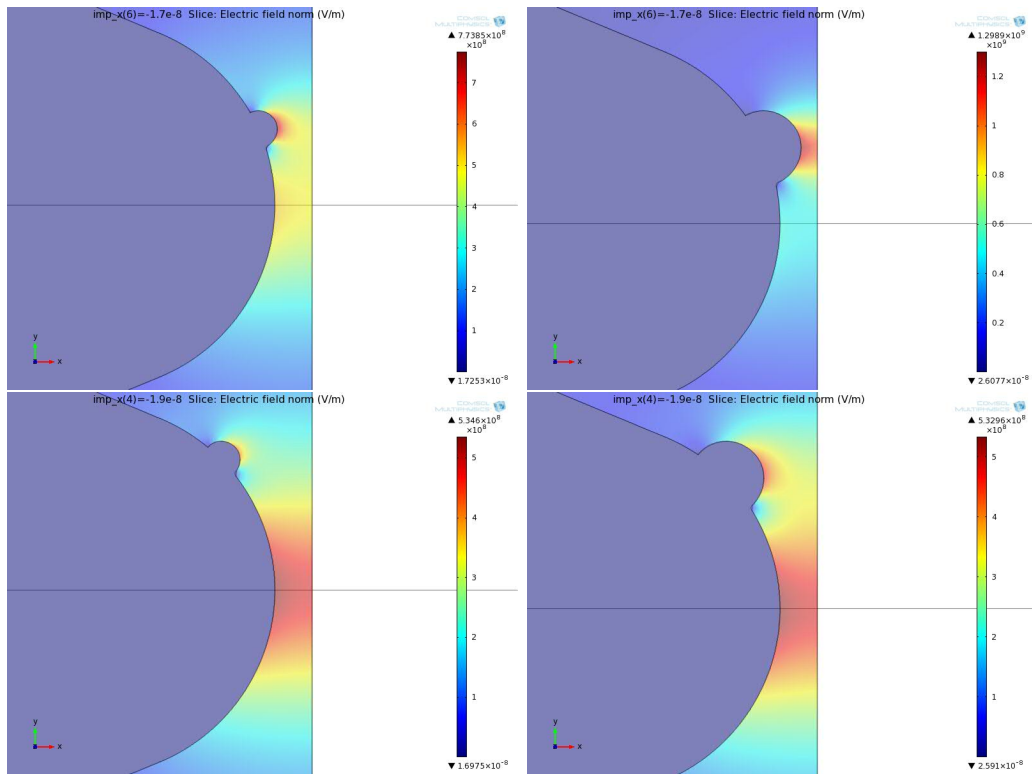


Figure 3.18: E-field magnitude surface plots with imperfection radius of  $1\text{nm}$  (left column) and  $2\text{nm}$  (right column) at various distances from the grounded edge

as predicted by the radius analysis, imperfections with smaller radiuses tend to increase the local electric field as well. The larger tip's electric field distribution does not necessarily follow its perfect ideal case, especially when the effective gap has been reduced. In summary, an increase in the electric field magnitude at the gap is observed when the imperfection decreases the ultimate gap width ( $\leq 2\text{nm}$ ) and the amount of enhancement is dependent on the tip radius, the smaller radius creating a larger E-field. This behavior is shown in Figure 3.19.

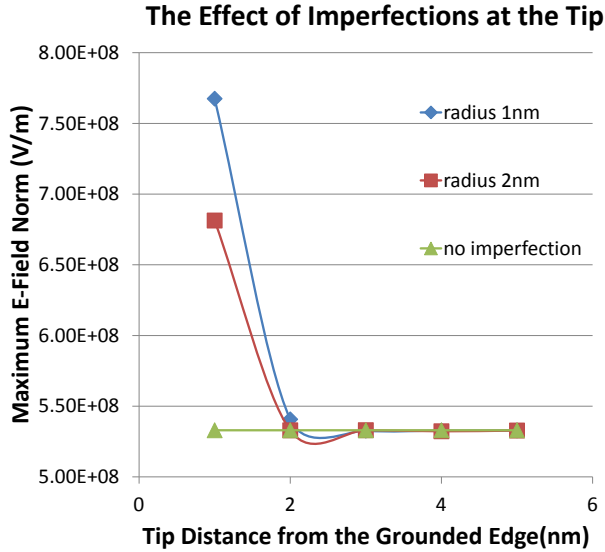


Figure 3.19: The effect of imperfections with tip radius of  $1\text{nm}$  and  $2\text{nm}$  on the maximum electric field

### 3.2 Electromagnetic Simulation Results

This section details the antenna performance of the ACMIM diode device through AC radiation coupling simulations. Once again, FEA was accomplished through COMSOL, although a different module was used (solving the three dimensional Maxwell equations) and the defined geometry was slightly different. As a function of frequency, the relative dielectric constant of nickel changes, and thus had to be incorporated into the material properties when frequency sweep simulations were run (values used from Palik et al. [17]). In the electrostatics module, a small air box encompassing the geometry was sufficient for accurate results. In this round of simulations, however, the propagating plane wave radiation is of great importance. To save on computation time, a Perfectly Matched Layer (PML) shell surrounded the antenna geometry, simulating an infinite domain. If designed cor-

rectly (one wavelength thick:  $10\mu\text{m}$ ), the PML will absorb any incident wave (such as reflections from the domain or antenna) and essentially acts as an open boundary condition. It is also important to make the entire domain surrounding the antenna (not counting the PML) a few wavelengths thick. In Figure 3.20, the complete geometry used in this set of simulations is shown, with the bow tie antenna located at the center of a  $20\mu\text{m}$  radius air sphere (2 wavelengths) and a  $10\mu\text{m}$  thick PML shell surrounding the air sphere.

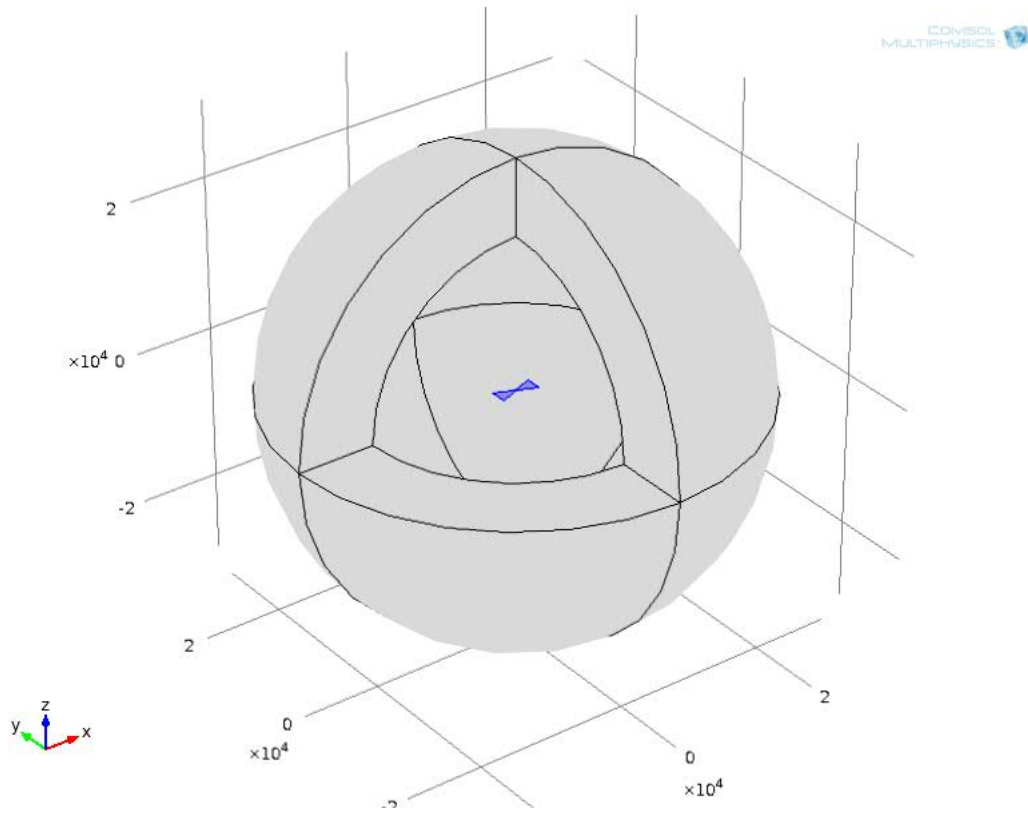


Figure 3.20: 3-D spherical simulation domain

The standard mesh density analysis was performed again since the geometry had changed (air spheres, PML shell), and the electromagnetic simulation requires smaller elements proportional to fractions of the incident radiation wavelength.

COMSOL recommends a maximum element size of less than  $1/5^{th}$  of the wavelength (in our case,  $2\mu m$ ) in order to capture the propagation behavior properly. As can be imagined in the geometry, the large air sphere itself forced the use of just under 1 million discrete elements, substantially increasing the computation time. The fact that the antenna tip had to be meshed much finer (like in the electrostatics simulations) complicated mesh generation considerably. The final mesh of just the antenna can be seen at different zoom levels in Figure 3.21.

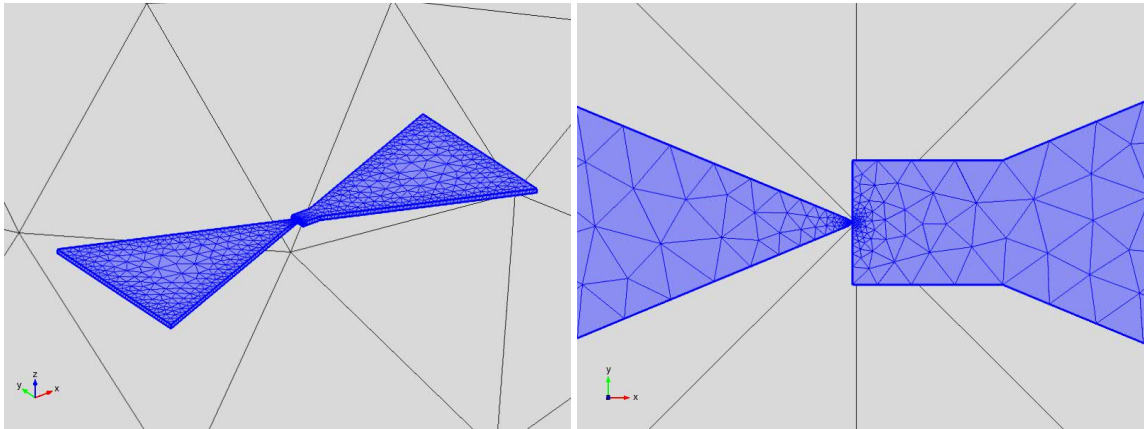


Figure 3.21: Mesh profile of the bow-tie antenna (left), focused view at the junction (right)

In addition to the mesh density analysis, a domain size analysis had to be done to confirm that changing the air sphere domain size did not affect the final results. Figure 3.22 shows that the chosen domain does well in allowing the background plane wave (electric field magnitude of  $1V/m$ ,  $10\mu m$  wavelength, x-direction polarization) to propagate with minimal distortion (even at the boundaries), and the PML shell absorbs any incident wave.

The particular geometry tested in this simulation had the parameters: half

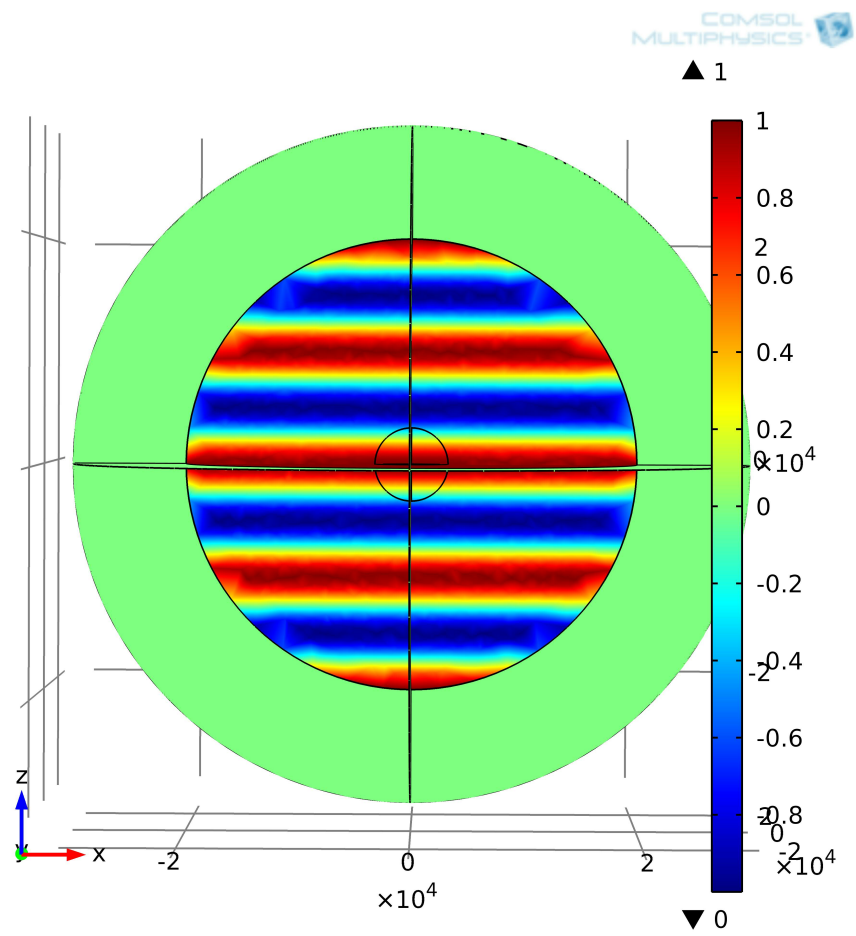


Figure 3.22: Plane wave of E-field magnitude  $1V/m$  and  $10\mu m$  wavelength, polarized in x-direction in the inner sphere air domain

antenna length  $L = 2.5\mu m$ , tip radius  $r = 10nm$ , flare angle  $\theta = 45^\circ$ , and gap width  $d = 2nm$ . In Figure 3.23, the two dimensional electric field magnitude distribution is shown (plane taken at half the antenna thickness). For an incoming wave of  $1V/m$ , the enhancement at the tip is approximately a factor of 4045. Figure 3.24 shows the same data, but at a further zoom level, and a scaled color axis from  $1V/m$  (red) to  $0V/m$  (blue), in order to portray the radiation pattern of the antenna.

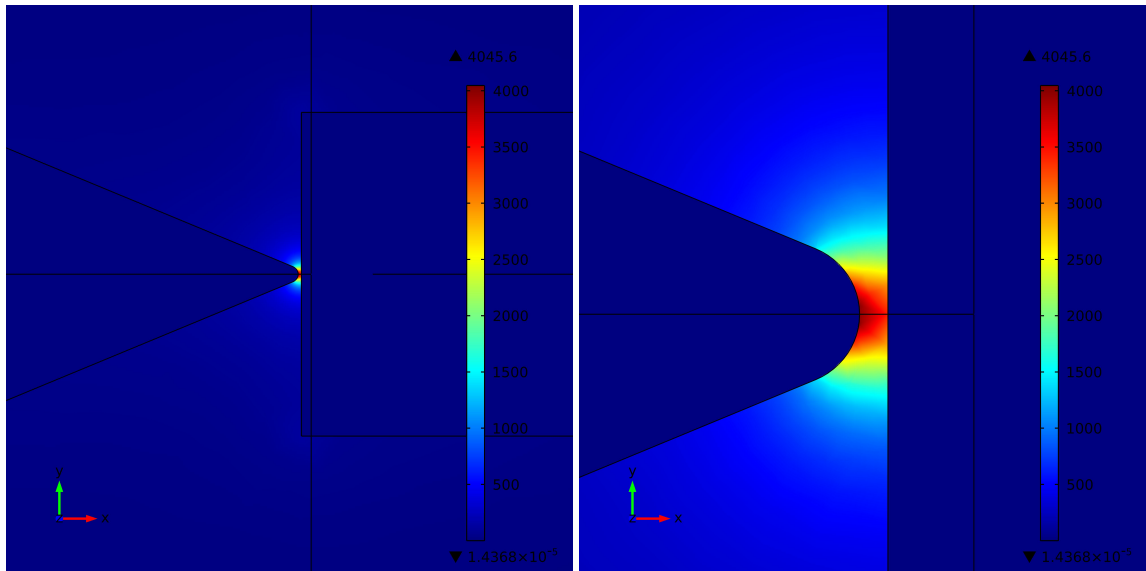


Figure 3.23: Antenna electric field magnitude distribution around the junction (left), focused view at the junction (right). Color scales from red ( $4045V/m$ ) to blue ( $0V/m$ )

### 3.2.1 Antenna Length Optimization

The next simulation varied the length of the antenna to find the optimal value. The designed antenna had a single side length of  $2.5\mu m$  based on dipole antenna theory that quotes a quarter wavelength as the optimum for resonance. However,

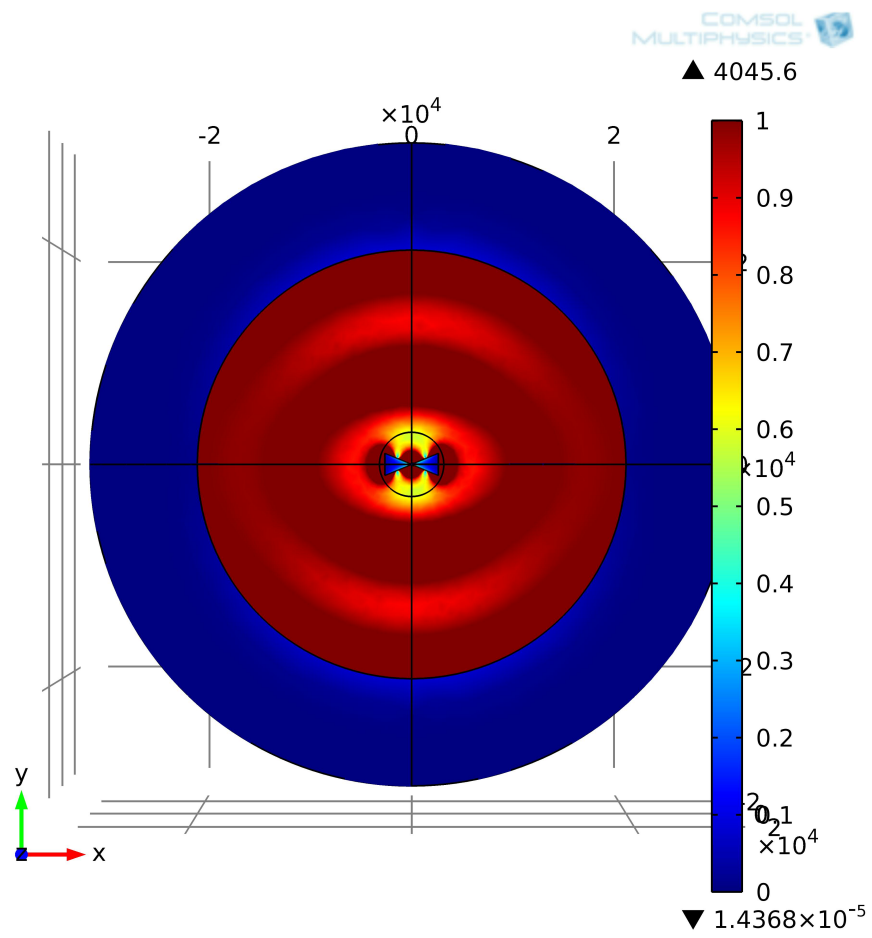


Figure 3.24: Rescaled antenna electric field distribution. Color scales from red (1 V/m) to blue (0 V/m)

with a bow tie antenna, the larger surface area (and metal thickness) can affect the resonant peak. A parametric simulation was run (at a frequency of  $30THz$ ) sweeping the half antenna length (and adjusting the geometry accordingly) from  $1\mu m$  to  $10\mu m$ , and the maximum electric field at the tip recorded as the comparison metric. The corresponding data can be found in Figure 3.25, which shows a peak at  $3\mu m$ , and another smaller peak at roughly  $6\mu m$ . This peak is very close to the designed value, and even with the sub-optimal design, the peak electric field is within approximately 10% of the maximum found at a half antenna length of  $3\mu m$ .

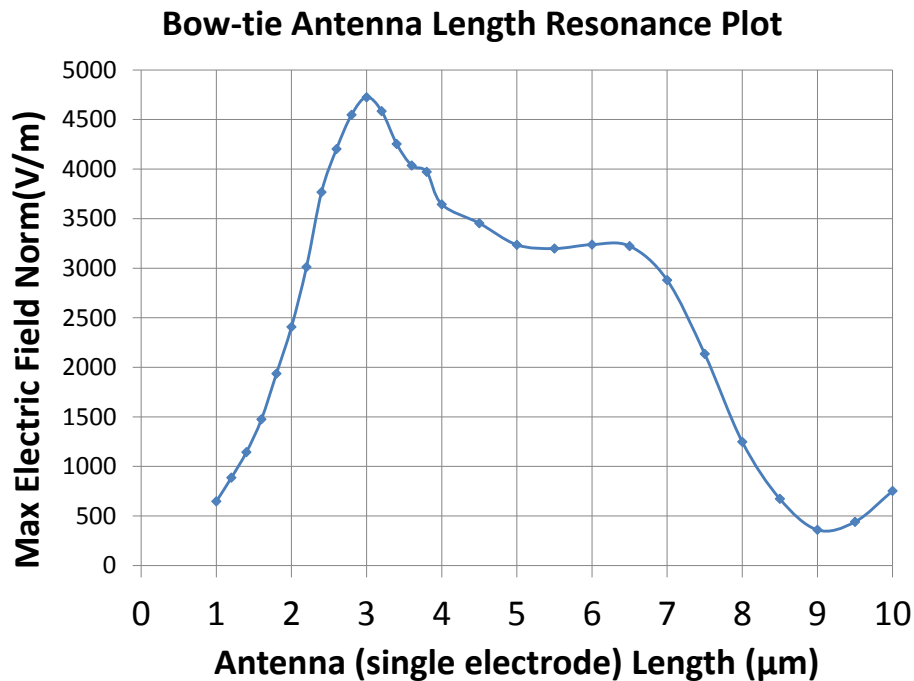


Figure 3.25: Maximum electric field magnitude vs. antenna half length

Continuing with the designed antenna of half length  $2.5\mu m$ , a parametric frequency was performed next, sweeping from  $10THz$  to  $50THz$ . The corresponding maximum electric field at the tip for each frequency is plotted in Figure 3.26. The

resonant peak is not quite at  $30\text{THz}$  as designed, but rather at about  $32.5\text{THz}$  (which can be predicted based on the antenna length simulations). From the plot, the antenna appears to have a large bandwidth (one of the design considerations), measured as roughly  $30\text{THz}$  across wavelengths from  $6.25\mu\text{m}$  to  $16.7\mu\text{m}$  (Full Width Half Maximum (FWHM) measurement).

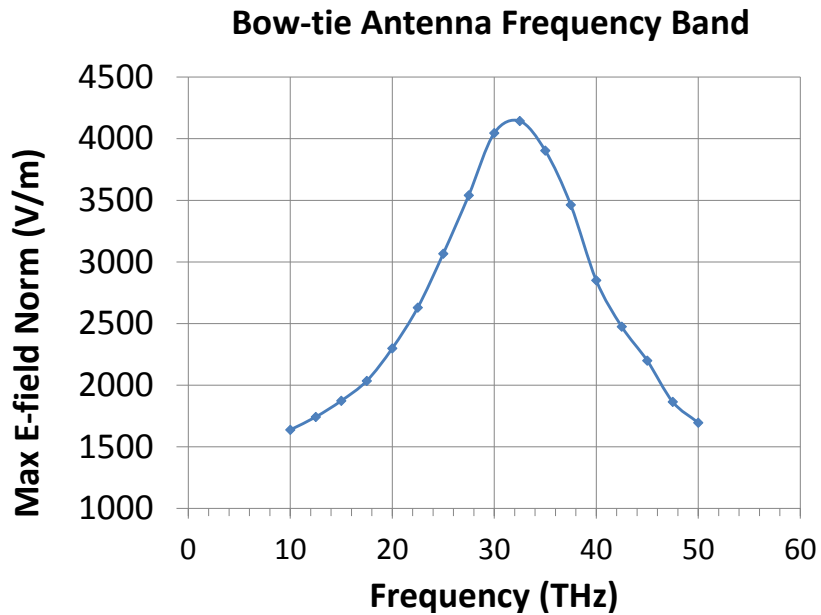


Figure 3.26: Frequency response of the  $2.5\mu\text{m}$  half length bow tie antenna

### 3.2.2 Polarization Effects

When attempting to couple unpolarized ambient energy from the environment, it is important to have an antenna that can effectively couple power from many angles. To test the polarization performance of the bow-tie antenna (same geometry as before), a parametric sweep was performed where the x and y components of the incoming radiation were varied (keeping the same overall magnitude though,

and traveling in the z direction still). This rotated the radiation in relation to the antenna's axis, and the maximum electric field at the tip was recorded at each specified angle. The corresponding values are plotted in Figure 3.27 where an imperfect sinusoid is seen (a dipole would have a perfect sinusoid polarization distribution). The maximum electric field at the tip drops below 50% of the peak ( $\leq 2000V/m$ ) for only  $120^\circ$  out of a total  $360^\circ$  range. Power is effectively coupled into the antenna over a wider range of angles for a bow tie antenna than a dipole (67% versus 50%), which enhances the energy harvesting capabilities of unpolarized IR radiation when using a bow tie antenna.

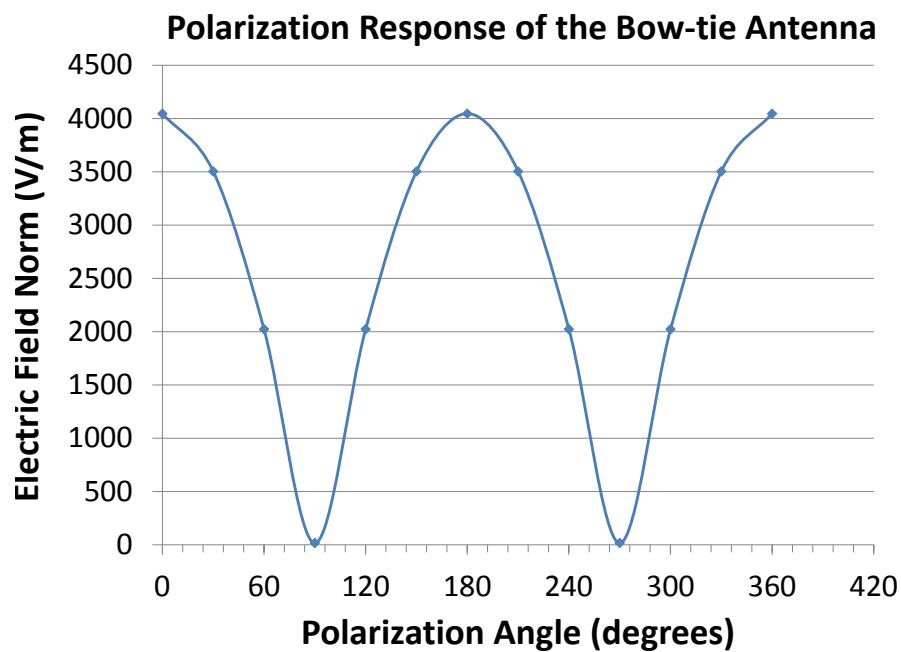


Figure 3.27: Polarization response of the bow tie antenna

### 3.2.3 Substrate and Air Coupling Comparison

These previous simulations have all assumed the antenna is floating in air, but in reality, the antenna is fabricated on a  $SiO_2$  insulating substrate. This introduces another medium and boundaries into the wave propagation, affecting the overall power coupling of the antenna. To simulate this, an oxide substrate disc is introduced to the geometric model, shown in Figure 3.28. The power coupling is expected to improve due to the wave propagation impedances matching better. With a bow tie antenna's impedance quoted to be around  $100\Omega$  to  $150\Omega$  (actually a function of flare angle [20, 6]), better matching can occur with the higher dielectric constant oxide ( $Z_{SiO_2} = 190\Omega$ ) than with free space ( $Z_0 = \sqrt{\mu_0/\epsilon_0} = 377\Omega$ ).

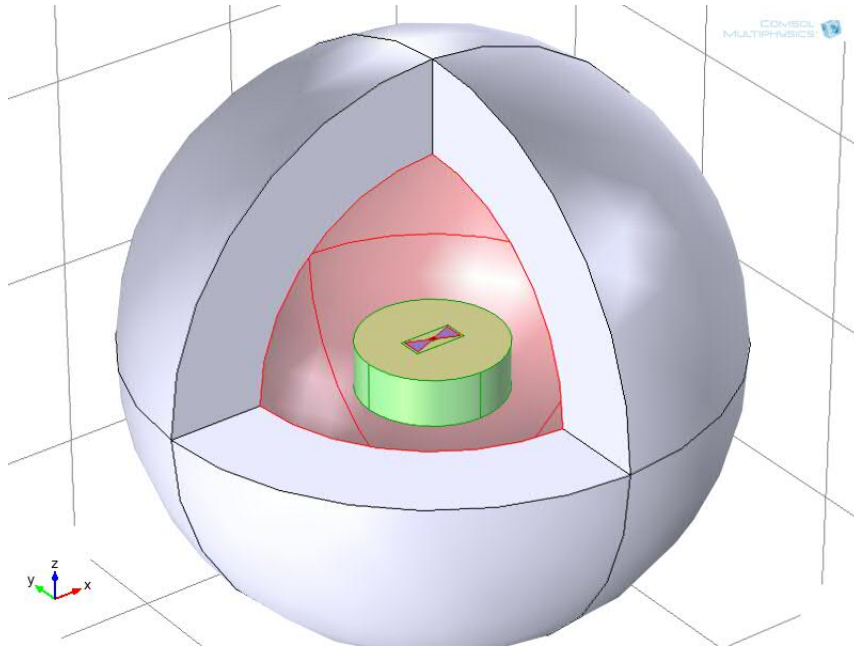


Figure 3.28: Geometry of ACMIM with substrate

With the addition of the oxide substrate, a propagating plane wave traveling in the positive or negative  $z$  direction would produce different power coupling because

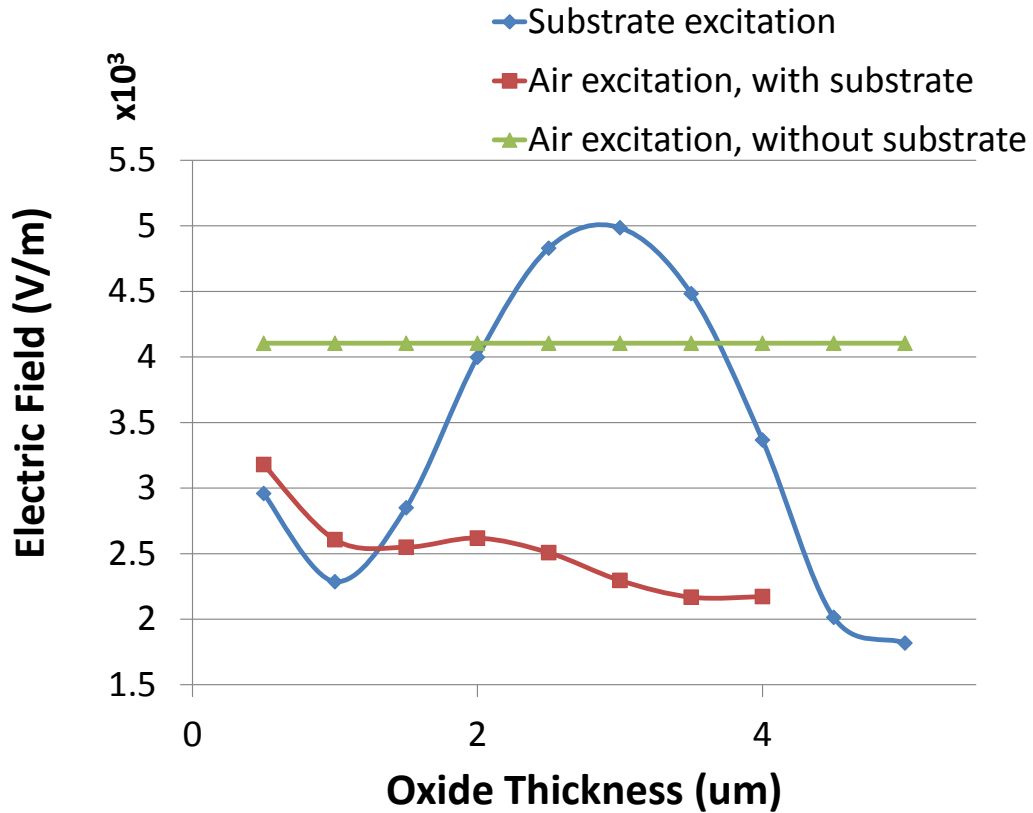


Figure 3.29: Max electric field magnitude as a function of oxide substrate thickness

the wave would encounter different impedances (in the previous simulations, the antenna is simply in air, thus the results for different propagation directions would be identical). Figure 3.29 compares the three cases: no substrate, propagation from the open air side, and propagation from the substrate side. The addition of the substrate always decreases the power coupling if the wave is propagating from the air side. However, if the wave propagates from the substrate side, it is possible to increase the electric field enhancement across the gap by almost 25% from roughly  $4000 \text{ V/m}$  to about  $5000 \text{ V/m}$  (this occurs at an oxide substrate thickness of  $3 \mu\text{m}$ ). This set of results shows that the energy harvesting capabilities of the antenna can

be further increased with a correctly designed medium.

### 3.3 Summary

According to the electrostatic simulation results:

- a small tip radius increases the electric field at the tip while decreasing the junction capacitance
- a narrow gap increases both the electric field and the junction capacitance
- flare angles less than  $120^\circ$  hardly affect the electric field, but do increase junction capacitance with larger flare angles
- imperfections at the tip can form hot spots that further enhance the electric field locally, especially when they are small in radius and close to the tip (or within the gap)
- Electric field is not constant across the gap, but rather peaks at the tip and decays non-linearly towards the flat edged electrode

According to the radiation coupling simulation results:

- for radiation of  $10\mu m$  wavelength, the antenna half length resonance occurs at  $3\mu m$
- for a half length of  $2.5\mu m$  antenna, the electric field enhancement is a factor of 4000

- a bow tie antenna with a  $45^\circ$  flare angle provides a minimum factor of enhancement of 2000 for a  $240^\circ$  polarization span (67%)
- a bow tie antenna with a  $45^\circ$  flare angle had a FWHM bandwidth of 30THz covering wavelengths from  $6.25\mu m$  to  $16.7\mu m$
- placing the antenna on an oxide substrate of thickness  $3\mu m$  and propagating the wave from that side can increase the electric field enhancement up to a factor of 5000

## Chapter 4

### Equivalent Circuit Model Simulation Results

This chapter presents the performance of the ACMIM diode from a circuit analysis perspective. Equivalent circuit models of both the antenna and diode are derived and simulated in PSpice. A shunt impedance across the diode is introduced into the model and its effects on performance noted in an attempt to understand the testing results discussed earlier.

#### 4.1 Equivalent Circuit Models

##### 4.1.1 Antenna

Antennas are historically modeled as an AC voltage source connected in series to an impedance. This impedance has both real and imaginary components that model the antenna's radiation resistance and resonant peaks. This series connection of the voltage source, resistance, capacitance, and inductance can be seen in Figure 4.1. If the antenna were designed correctly for a given frequency  $f$  and quality factor  $Q$ , the circuit component values can be derived from Equation 4.1.

$$2\pi f = \frac{1}{\sqrt{L_A C_A}} \quad \text{and} \quad Q = \frac{1}{R_A} \sqrt{\frac{L_A}{C_A}} \quad (4.1)$$

For the bow tie antenna, the real component of the antenna impedance is the

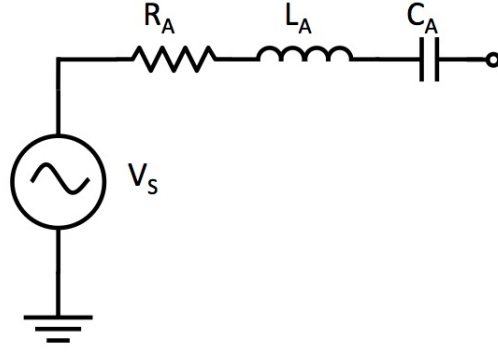


Figure 4.1: Equivalent circuit model of the designed bow tie antenna

radiation resistance, which has been found to be a function of the flare angle [6, 20]. For flare angles between  $5^\circ$  and  $100^\circ$ , the resistance can vary between  $200\Omega$  and  $50\Omega$ , as shown in Figure 4.2. For the fabricated flare angles and rest of this discussion, the value of  $R_A$  was set to be  $100\Omega$ . Assuming a quality factor of about 4, the values of  $C_A$  and  $L_A$  can be determined from Equation 4.1. For a resonant frequency of  $30\text{ THz}$ , the antenna's capacitance works out to be  $13.3\text{ aF}$  and the inductance is  $2.128\text{ pH}$ .

#### 4.1.2 Diode

The diode element can be modeled by a nonlinear, bias dependent resistance and a capacitance in parallel, as seen in Figure 4.3 (a shunt resistance would also be added in parallel). The resistance value is derived from  $\frac{dV}{dI}$  of the tunneling current-voltage relation plot. When modeling the resistance for simulations using PSpice, a voltage controlled current source with a polynomial fit of the current is used. Since this models the tunneling current, the derived fifth order polynomial fit is taken

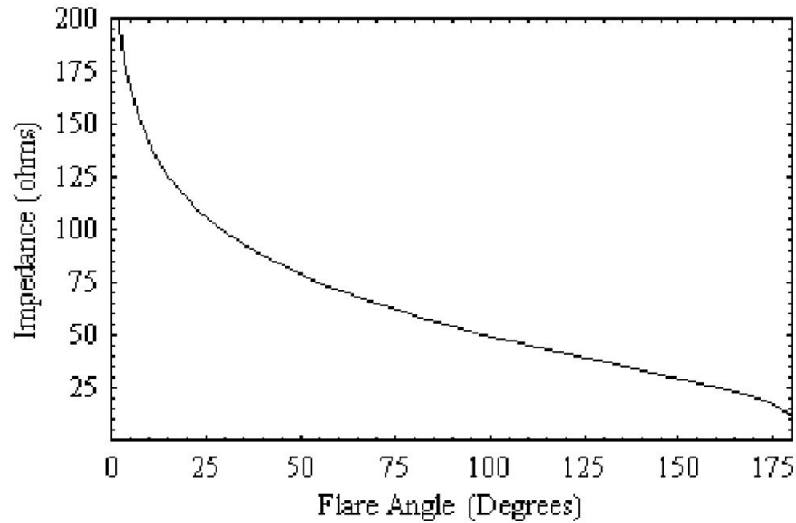


Figure 4.2: Bow tie antenna resistance versus flare angle (from [6])

from the initial parameter analyzer test (when the device is still nonlinear). The capacitance value is taken from the COMSOL simulations presented earlier. For these circuit simulations, a geometry was assumed that gave a capacitance value of approximately  $30aF$ . It should be noted that this is just an estimate derived from numerical methods, and there is no simple way to experimentally measure the capacitance of the MIM structure. This is an important parameter that affects the device's performance, especially the frequency response behavior.

### 4.1.3 ACMIM with Measurement

The entire circuit, along with biasing and measurement components can be seen in Figure 4.4. To bias the diode for maximum responsivity (at approximately  $100mV$ ), a voltage source  $V_B$  and resistor (value equivalent to the parallel combination of the diode and shunt resistances) is inserted at the node between the diode

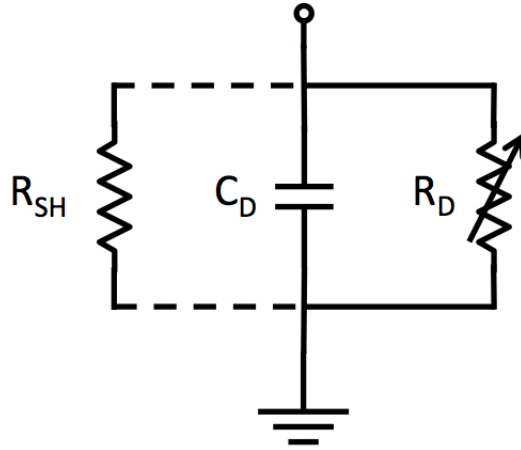


Figure 4.3: Equivalent circuit model of the MIM diode

and antenna. This fixes the DC voltage at the node based on the divider ratio, and any AC signal from the antenna oscillates around this potential. For the measurement circuit, an op-amp with a feedback resistor is used to amplify the very small currents (nanoamp order of magnitude) into more measurable voltages. To find the rectified DC current levels, the fast fourier transform (FFT) of the output trace is taken, and the  $0Hz$  component is used.

## 4.2 Shunt Resistance

The filaments formed by electric field migration give rise to alternate current paths in addition to the tunneling current. As an actual conductive metallic path through the oxide, they can be modeled as a simple resistor in parallel with the other modeled elements of the diode (forward resistance and capacitance). One of the first circuit simulations ran computed the current-voltage relationship for the polynomial fit in parallel with the shunt resistance (value of  $750\Omega$ ), which can be

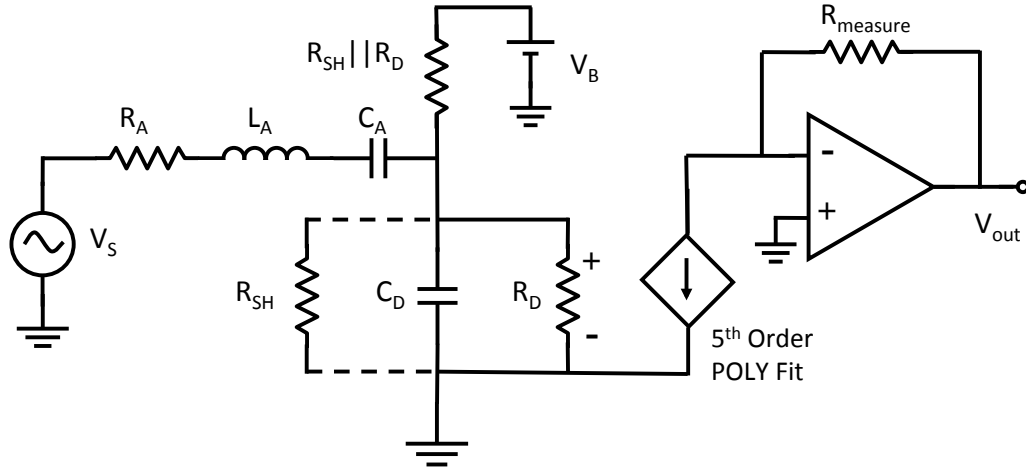


Figure 4.4: Equivalent circuit model of the entire ACMIM structure, with biasing and measurement

seen in the plot of Figure 4.5. The blue trace shows the nonlinear tunneling current, while the red trace shows the linear shunt resistance current. The final trace (green) on the plot shows the summation of these two currents, giving rise to a practically linear relationship. This form of the plot matches the device behavior seen during the testing of previously fabricated devices.

### 4.3 Impedance Matching

In order to effectively transfer power from one stage in a circuit to another, their conjugate impedances should be as close as possible. If two stages do not have similar real and opposite sign imaginary impedance components, a matching network can be inserted to transform the impedance looking into a stage and force it to match the previous stage. Many radiation energy harvesting systems, such

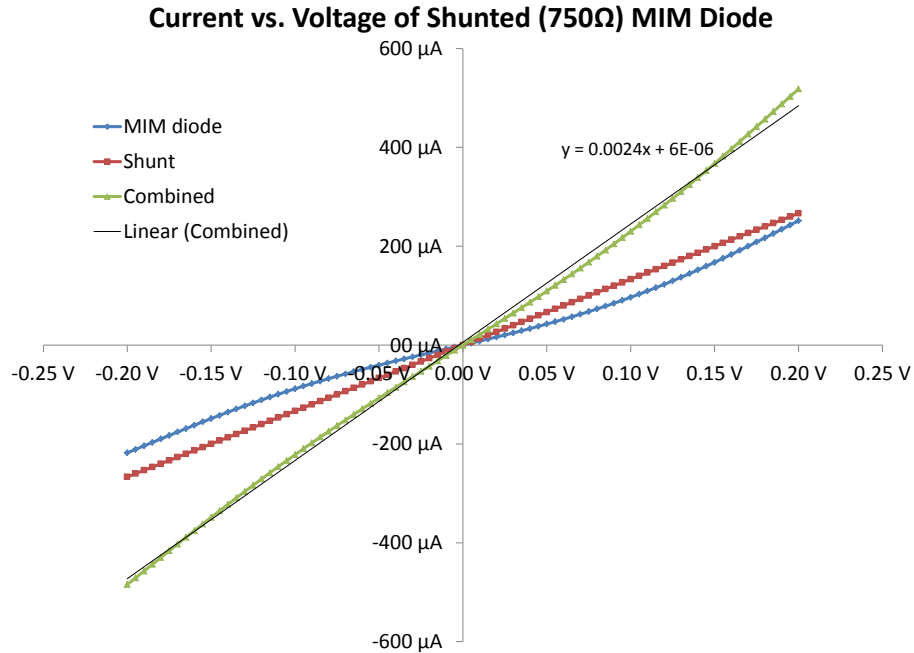


Figure 4.5: Current versus voltage relationship showing tunneling, shunt, and overall currents

as the one pictured in Figure 4.6, are implemented on a much more macro scale, and do not involve a single integrated diode/antenna structure. The single ACMIM structure and the very small dimensions we are working with do not allow for the insertion of an external impedance matching network (like the one in Figure 4.6). This limits the efficiency of power harvesting because the power is not being fully coupled into the diode for rectification.

Without the ability to insert a matching network, there seems to be little that can be done to improve the power coupling. However, with a shunt resistance across the MIM diode, the effective impedance of the diode changes (the diode resistance and shunt are now in parallel, reducing the total resistance). Equation 4.2 describes the antenna's impedance, while Equations 4.3 and 4.4 details the impedance of the

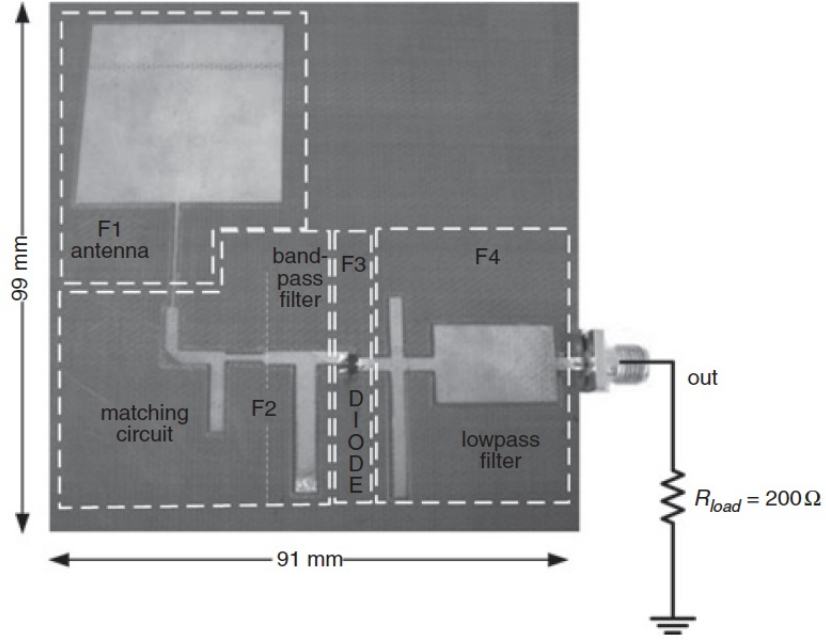


Figure 4.6: Energy harvesting circuit designed for 2.45 GHz radiation, with matching network (from [4])

diode without the shunt, and with its introduction, respectively. Depending on the shunt resistance, it could be possible to achieve a better matching configuration. To explore this, a script was written in MATLAB that swept the shunt resistance and plotted the magnitude as well as the real and imaginary components of the diode impedance, comparing it to that of the antenna's.

$$Z_A = R_A + j\omega L_A + \frac{1}{j\omega C_A} \quad (4.2)$$

$$Z_D = \left( \frac{1}{R_D} + j\omega C_D \right)^{-1} \quad (4.3)$$

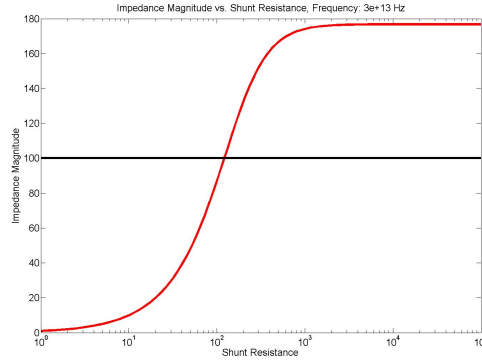
$$Z_D = \left( \frac{1}{R_D} + \frac{1}{R_{SH}} + j\omega C_D \right)^{-1} \quad (4.4)$$

Table 4.1: Impedance components of antenna and unshunted diode

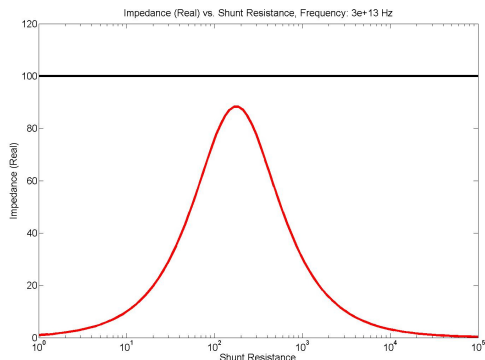
Element	Magnitude ( $\Omega$ )	Real ( $\Omega$ )	Imaginary ( $\Omega$ )
Antenna	100.027	100	2.234
Diode (no shunt)	176.839	0.045	-176.839

As seen in the plots of Figure 4.7, the magnitudes and both real and imaginary components of the diode (red) can vary widely depending on the present shunt resistance (plots shows shunts from  $1\Omega$  to  $100k\Omega$ ). For reference, the values of the antenna's impedance components and the unshunted diode's impedance components are listed in Table 4.1 (note: diode forward resistance taken as  $700k\Omega$ ). The table shows a large matching problem. In the ideal case, the real components would be equal, and the imaginary components would be conjugates of each other (giving equal overall magnitudes as well). Although the overall impedance magnitudes are similar (same order of magnitude), the real components are drastically different ( $100\Omega$  versus  $< 1\Omega$ ), as well as the imaginary components ( $2\Omega$  versus  $-177\Omega$ ). Large mismatch in the components will cause very inefficient power coupling from the antenna to the diode, hurting the overall system rectification performance.

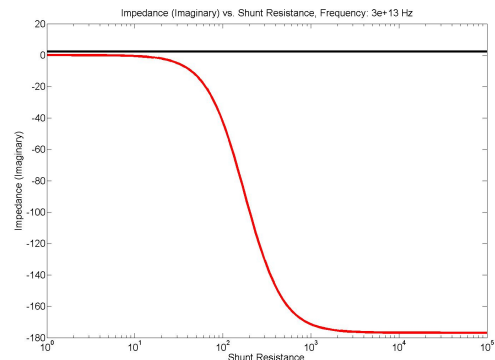
From Figure 4.7, it is obvious that the introduction of the shunt resistance can in fact improve the matching of the antenna to the diode. As an example, take the antenna's real impedance component of  $100\Omega$ . With a shunt of around  $200\Omega$ , the real component of the diode impedance can be as large as  $88\Omega$ . Comparing that value to the unshunted diode in Table 4.1 of  $0.045\Omega$ , it is clear that this is a huge



(a) Magnitude of impedances



(b) Real components



(c) Imaginary components

Figure 4.7: Comparison of diode (red) and antenna (black) impedance components for varying shunt resistances

improvement when trying to match  $100\Omega$ . Using this same shunt value, the imaginary impedance component is about  $-93\Omega$ , matching better to the roughly  $2\Omega$  of the antenna (compared to  $-177\Omega$  without the shunt). It is clear from the imaginary plot that a better matching imaginary component can be achieved with a smaller shunt. This however, will reduce the matching ability of the real component just discussed, so it becomes clear that there exists some optimum value of shunt resistance to achieve the best matching. It should also be noted that shunt resistances

all the way up into the  $5k\Omega$  range can still provide a small matching benefit.

To verify these calculations, a circuit simulation was run in PSpice measuring the average power from the AC source, and the average power coupled into the diode for a wide range of shunt resistances. The power levels measured in this simulation can be seen in Figure 4.8, where the blue line represents the source power while the red line shows the power coupled into the diode. At low shunt impedances, the diode is effectively shorted, and the power the source provides to the circuit is only for the antenna. At higher shunt values, the power the source needs to supply includes the diode, which is why it rises and eventually levels off (effective impedance of diode changes little with large values) as a function of shunt resistance. From the plot and analyzing the data, we can observe that the greatest power coupled across the diode occurs roughly between  $75\Omega$  and  $750\Omega$ , which agrees well with the predicted values determined through impedance calculations. In comparison to the source power, the maximum power coupled across the diode was 41%, much more than the fractions of a percentage point in the no shunt case. This increase in power is evident in the plot and as a result of the extra power coupled into the diode, more rectified power will be delivered. During processing, if this shunt impedance can be controlled (though different oxidation or anodization methods), better performing ACMIM structures can be fabricated that take into account this optimization.

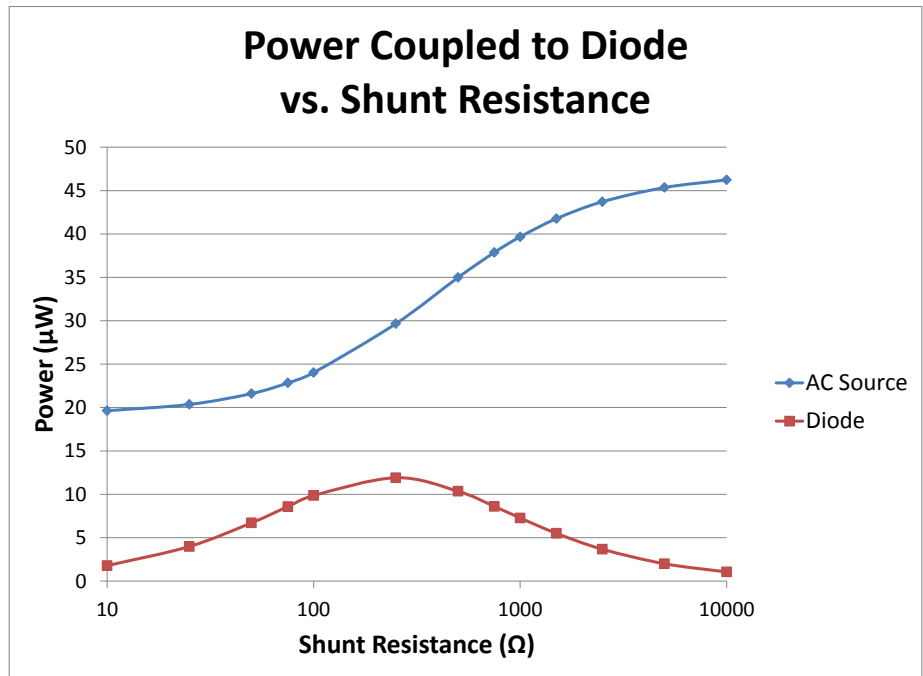


Figure 4.8: Plot of the source power (blue) and power coupled into the diode (red) as a function of shunt resistance

#### 4.4 Frequency Response

When a shunt resistance is added in parallel to the diode’s resistance, the effective resistance of the diode is lowered, helping the frequency response of the device due to the smaller RC time constant of the junction. At the same time, an impedance divider ratio between the diode and antenna exists, and this lower resistance reduces the ratio, resulting in less voltage coupled across the diode. Too small of a shunt resistance results in low coupling due to the divider ratio, while too large results in low coupling due to the frequency response (diode cutoff pole is not moved close enough to the operating frequency). There exists some optimal shunt resistance for this frequency response versus impedance divider ratio tradeoff, shown

in Figure 4.9. This plot only takes into account two efficiency factors: the divider ratio and decay of response past the frequency cutoff. Of course, other parasitics may come into play, but this computational result at least establishes a possible explanation of the observed behavior.

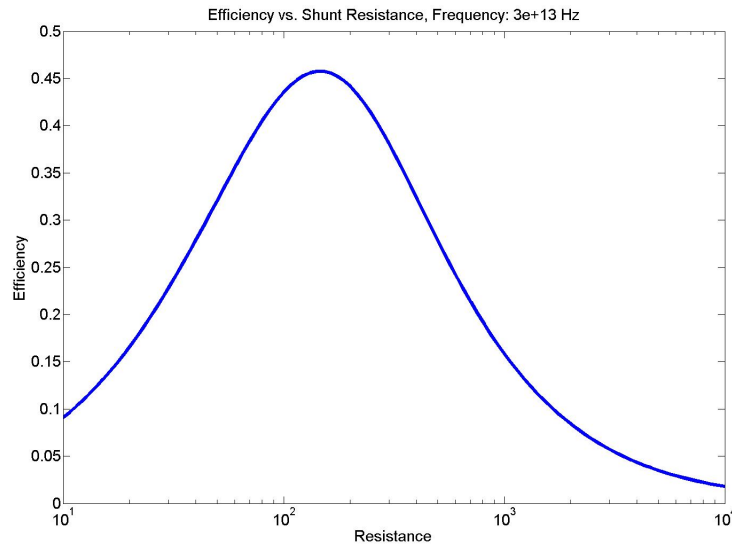


Figure 4.9: Plot of efficiency versus shunt resistance. Left decay from divider ratio, right decay from frequency response

This optimal shunt resistance behavior is likely to only occur with junctions whose RC time constant limited frequency cutoff is near the operating frequency. This is because large shunt impedances can move the pole just enough without the divider ratio taking a huge hit. A function whose cutoff is higher than the operating frequency should not be helped by the shunt since it will only harm the divider ratio (by reducing the effective resistance) while any frequency improvements are not necessary. In the opposite case where the junction cutoff frequency is very much below the operating frequency (like our device discussed later in this section),

only small shunts move the pole sufficiently, but destroying the divider ratio at the same time. For this reason, the case where the diode resistance and capacitance were  $200k\Omega$  and  $1 \times 10^{-19}F$ , respectively, was simulated in PSpice first. This diode parameter combination gives a cutoff frequency of approximately  $8 THz$ , allowing some room for manipulation of the diode's cutoff frequency using fairly large shunt resistances at a  $35 THz$  operating frequency.

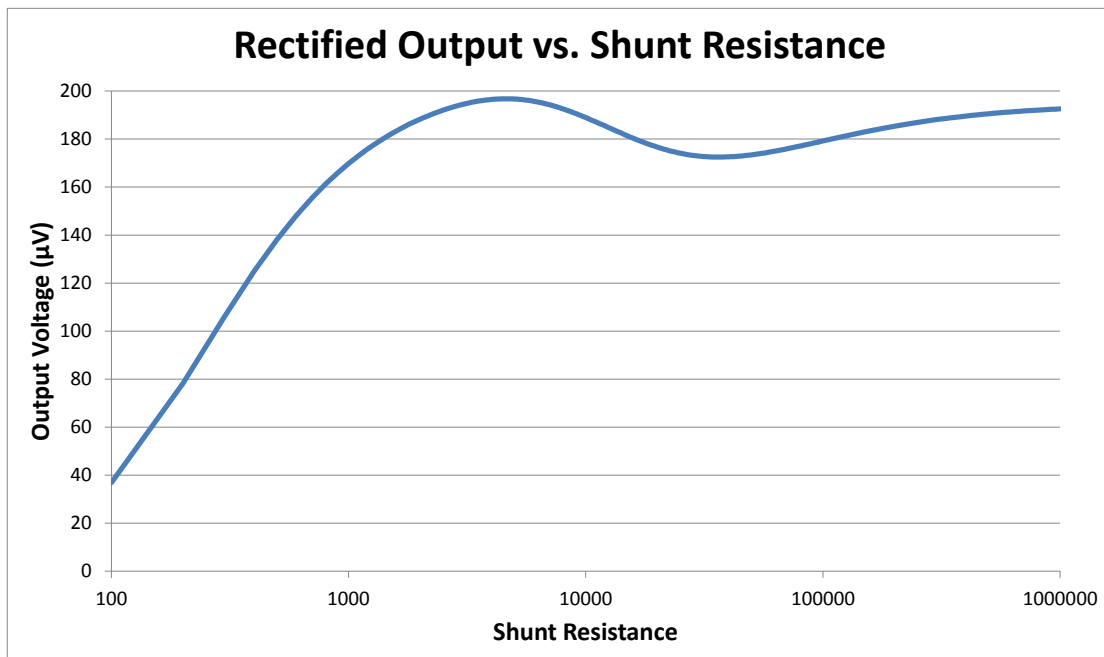


Figure 4.10: Plot of output voltage versus shunt resistance. Observe the slight peaking behavior around  $5k\Omega$

In Figure 4.10, the output voltage from the measurement circuit is plotted against the shunt resistance. This plot does show some of the expected peaking behavior giving an optimal shunt value somewhere in the neighborhood of  $5k\Omega$ , but

then the output rises again to asymptotically approach the no shunt case. This large valued shunt behavior was not predicted by the simple two factor estimation shown previously, but does make sense because larger (infinite) shunts emulate the no shunt case. This diode was unbiased, and the simulations for the biased case show the same peaking behavior, but much less pronounced and at a higher shunt ( $20k\Omega$  range).

It should be noted however, that this tradeoff behavior, while interesting, does not fully explain the increase in performance that the linear devices showed during testing. At the optimum shunt value around  $4.6k\Omega$ , the output voltage was  $196.777\mu V$ , compared to the no shunt value of  $194.749\mu V$ , hardly a statistically significant improvement, and nowhere near the experimentally observable gains. Also, this behavior was for a completely unrealistic set of diode resistance and capacitance, and simulations using the believed parameters had a vastly different behavior.

When the simulations were run using a forward resistance of  $700k\Omega$  and a capacitance of  $30aF$ , this general peaking behavior was not observed at all, with the output voltage as a function of shunt resistance a monotonically increasing plot. This combination of diode resistance and capacitance gave a cutoff frequency of around  $7.6 GHz$ , so in order to move the pole to a respectable frequency, a very small shunt impedance was needed, substantially reducing the divider ratio. Thus the frequency benefits were completely offset by the divider ratio tradeoff in this case, and the best case scenario is without a shunt.

Comparing the results from these two possible scenarios (impedance matching

and the frequency response versus divider ratio) can help explain why we were seeing an increase in performance experimentally. While the sensitivity may not have seen an improvement (this would be as a result of the frequency response versus impedance divider tradeoff), the overall localization of power and the better impedance matching conditions would give more rectified output power. When talking about sensitivity, we are concerned with the amount of voltage coupled across the diode (hence we want the large divider ratio but minimal attenuation through the RC time constant). When talking about impedance matching, we are concerned with the amount of power coupled into the diode, as larger amounts of available power for rectification (supplied by the antenna) results in larger rectified output power amounts. With better matching, the power will also be more localized to the junction since there will be less reflections and a higher percentage of total rectenna power is found in the diode. The addition of the shunt can help improve the impedance matching, increasing the power output performance metric, but it did not help with the sensitivity.

## 4.5 Summary

- Equivalent circuit models for the antenna and diode, as well as the entire ACMIM with biasing and measurement circuits were presented.
- The effect on the diode's current-voltage relationship (linearization) due to the filaments caused by field forming is discussed and plotted.
- The possible benefit of the shunt resistance on impedance matching of the

antenna and diode was modeled.

- At the optimal shunt resistance value, a maximum of 41% of power can be coupled across the diode, in comparison to  $< 1\%$  in the no shunt case.
- The tradeoffs between improved frequency response and impedance divider ratio were discussed.
- The optimization of this tradeoff for given sets of diode parameters was determined through PSpice simulations.
- The improved performance of the linearized devices was determined to be from impedance matching. For realistic diode parameters, power coupling could be greatly increased, while the frequency/divider ratio tradeoff was unable to produce any gains (RC time constant too large).

## Chapter 5

### Conclusions and Suggestions for Further Work

In this thesis, the design and simulation of a Ni/NiO<sub>x</sub>/Ni ACMIM tunnel diode structure suitable for infrared energy harvesting and detection has been presented. The design integrates geometric asymmetry at the junction to induce a current-voltage relationship asymmetry, through the use of electric field enhancement.

The device geometry was optimized using a commercial finite element analysis software, COMSOL Multiphysics. The simulations examined the effect on the electric field enhancement of the tip radius of curvature, flare angle, gap width, as well as imperfections near the tip. The capacitance change with each of the geometric variations was also noted, proving how the electric field enhancement decouples the capacitance and resistance of the MIM junction (capacitance values were around  $30aF$ ). From the simulations, it is clear that a sharp, small radius of curvature tip has the greatest effect on the electric field, and thus the rectification performance.

The antenna characteristics of the ACMIM structure were also analyzed using COMSOL. For just the antenna surrounded by air, optimal coupling of radiation at a  $10\mu m$  wavelength occurred for antenna half lengths of  $3\mu m$ , with an electric field enhancement factor of over 4000. The results confirmed the broadband trait of a bow tie antenna, with a  $30 THz$  FWHM bandwidth from wavelengths of  $6.25\mu m$  to  $16.7\mu m$ . Also confirmed was the wide polarization angle of  $240^\circ$  with over 50%

of the maximum electric field enhancement. The antenna on a dielectric substrate was also tested, showing an even higher electric field enhancement at the optimal substrate thickness.

Equivalent circuit models of the antenna and diode were developed and simulated in an attempt to reconcile testing result inconsistencies. Devices had started with nonlinear current-voltage relationships and responded to IR radiation, but afterwards had become visibly linear, yet those same devices responded better to incident radiation. The cause of the linearization of the diode comes from electric field formed filaments, or shunts. Modeling opens the possibility the the addition of these shunts improves matching of the antenna and diode impedances. This would give rise to more power coupled across the diode and higher rectification efficiency.

**Future Work:** There are numerous paths of research that can be undertaken to advance the state of ACMIM diode technology. The first involves current processing steps, namely the nickel deposition process and subsequent oxidization. The COMSOL simulations showed how important an extremely sharp (narrow radius) tip is to the field enhancement necessary for rectification. However, during processing, the grain size of the nickel limits the smallest achievable tip radius. Switching to a cryogenic deposition process to create an amorphous nickel structure could help obtain smaller tips, giving rise to better rectification performance. Another processing improvement involves the oxide layer. A robust and exact dimensioned insulating layer is crucial to device performance. The current oxidation method (low power  $O_2$  plasma) induces too much variability into the devices, and does not allow precise control over the thickness and composition of the oxide layer. Investigating

anodic oxidation techniques (among other alternate oxidation methods) could allow for more stable and robust oxides that have less variability amongst devices. Ideally, we would also like to be able to control the shunt impedances through oxidation methods as well in order to achieve the best matching scenario.

Eventually, arrays of these ACMIM devices would need to be created to harvest any appreciable power. Investigations into the ideal configuration (series and parallel combinations of devices) to obtain the maximum power output would need to be undertaken. Variability in the devices could drastically affect the overall performance of the network, thus they need to be taken into account carefully here. A related study would also need to be performed through COMSOL studying the effects of nearby antennas in the array on radiation coupling performance.

## Bibliography

- [1] Berland B., Simpson L., Nuebel G., Collins T., and Lanning B.. Optical rectenna for direct conversion of sunlight to electricity. *In National Center for Photovoltaics Program Review Meeting.*, pages 323–324, 2001.
- [2] Kwangsik Choi, Geunmin Ryu, Filiz Yesilkoy, Athanasios Chryssis, Neil Goldman, Mario Dagenais, and Martin Peckerar. Geometry enhanced asymmetric rectifying tunneling diodes. volume 28, pages C6O50–C6O55. AVS, 2010.
- [3] Kwangsik Choi, F. Yesilkoy, Geunmin Ryu, Si Hyung Cho, N. Goldman, M. Dagenais, and M. Peckerar. A focused asymmetric metal-insulator-metal tunneling diode: Fabrication, dc characteristics and rf rectification analysis. *Electron Devices, IEEE Transactions on*, 58(10):3519–3528, Oct.
- [4] A. Douyere, J.-D.L.S. Luk, and F. Alicalapa. High efficiency microwave rectenna circuit: modelling and design. *Electronics Letters*, 44(24):1409–1410, 2008.
- [5] R. H. Fowler and L. Nordheim. Electron Emission in Intense Electric Fields. *Royal Society of London Proceedings Series A*, 119:173–181, May 1928.
- [6] F.J. Gonzalez and G.D. Boreman. Comparison of dipole, bowtie, spiral and log-periodic ir antennas. *Infrared Physics and Technology*, 46(5):418 – 428, 2005.
- [7] S. Grover and G. Moddel. Applicability of metal/insulator/metal (mim) diodes to solar rectennas. *Photovoltaics, IEEE Journal of*, 1(1):78–83, July.
- [8] Thomas E. Hartman. Tunneling of a wave packet. *Journal of Applied Physics*, 33(12):3427–3433, 1962.
- [9] Philip C. D. Hobbs, Robert B. Laibowitz, and Frank R. Libsch. Ni-nio-ni tunnel junctions for terahertz and infrared detection. *Appl. Opt.*, 44(32):6813–6822, Nov 2005.
- [10] Philip C. D. Hobbs, Robert B. Laibowitz, Frank R. Libsch, Nancy C. LaBianca, and Punit P. Chiniwalla. Efficient waveguide-integrated tunnel junction detectors at 1.6  $\mu\text{m}$ . *Opt. Express*, 15(25):16376–16389, Dec 2007.
- [11] Bailey R. L. A proposed new concept for a solar- energy converter. *Journal of Engineering for Power*, 73, April, 1972.
- [12] Stepan Lucyszyn. Microwave characterization of nickel. *PIERS Online*, 4(6):686–690, 2008.
- [13] R. A. Millikan and Carl F. Eyring. Laws governing the pulling of electrons out of metals by intense electrical fields. *Phys. Rev.*, 27:51–67, Jan 1926.

- [14] N.M. Miskovsky, S. J. Shepherd, P.H. Cutler, T.E. Sullivan, and A. A. Lucas. The importance of geometry, field, and temperature in tunneling and rectification behavior of point contact junctions of identical metals. *Applied Physics Letters*, 35(7):560–562, 1979.
- [15] Moichiro Nagae. Response time of metal-insulator-metal tunnel junctions. *Japanese Journal of Applied Physics*, 11(11):1611–1621, 1972.
- [16] Lothar Nordheim. Zur theorie der thermischen emission und der reflexion von elektronen an metallen. *Zeitschrift fur Physik*, 46(11-12):833–855, 1928.
- [17] Edward D. Palik. *Handbook of Optical Constants of Solids*. Academic Press, 1985.
- [18] Juraj Racko, Miroslav Mikolek, Ralf Granzner, Juraj Breza, Daniel Donoval, Alena Grmanov, Ladislav Harmatha, Frank Schwierz, and Karol Frhlich. Trap-assisted tunnelling current in mim structures. *Central European Journal of Physics*, 9:230–241, 2011.
- [19] A. Rogalski. Infrared detectors for the future. *Acta Physica Polonica A*, 116(3):389, 2009.
- [20] D.B. Rutledge and Michael S. Muha. Imaging antenna arrays. *Antennas and Propagation, IEEE Transactions on*, 30(4):535–540, Jul.
- [21] R.A. Sayer, Juan Zeng, Hao-Han Hsu, D. Peroulis, and Timothy S. Fisher. Thermal and electrical conductivities of nanocrystalline nickel microbridges. *Microelectromechanical Systems, Journal of*, 21(4):850–858, 2012.
- [22] W. Schottky. uber kalte und warme elektronenentladungen. *Zeitschrift fur Physik*, 14(1):63–106, 1923.
- [23] X. Shao, N. Goldsman, N. Dhar, F. Yesilkoy, A. Akturk, S. Potbhare, and M. Peckerar. Simulation study of rectifying antenna structure for infrared wave energy harvesting applications. In *Proceedings of SISPAD*, pages 249–252, Denver, CO, USA, September 2012.
- [24] J G Simmons. Conduction in thin dielectric films. *Journal of Physics D: Applied Physics*, 4(5):613, 1971.
- [25] John G. Simmons. Generalized formula for the electric tunnel effect between similar electrodes separated by a thin insulating film. *Journal of Applied Physics*, 34(6):1793 –1803, jun 1963.
- [26] John G. Simmons. Generalized thermal j-v characteristic for the electric tunnel effect. *Journal of Applied Physics*, 35(9):2655–2658, 1964.
- [27] Filiz Yesilkoy. *IR Detection and Energy Harvesting Using Antenna Coupled MIM tunnel Diodes*. PhD thesis, University of Maryland College Park, 2012.